TÉCNICO LISBOA

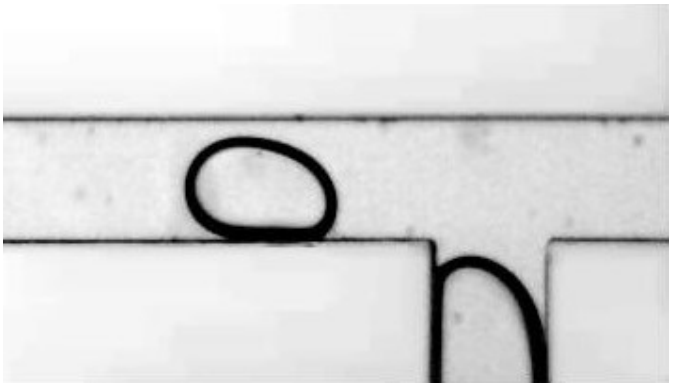

Microdroplet formation and flow characteristics of water and nanofluids in microfluidic channel

André Filipe Loureiro Governo

Thesis to obtain the Master of Science Degree in

Mechanical Engineering

Supervisors: Prof. Sohel Murshed
Prof. Viriato Sérgio de Almeida Semião

Examination Committee

Chairperson: Prof. Carlos Frederico Neves Bettencourt da Silva
Supervisor: Prof. Sohel Murshed
Member of the Committee: Prof. Susana Isabel Pinheiro Cardoso de Freitas

November 2019

Acknowledgments

The first words of appreciation should be directed towards my supervisors. I want to thank professor Sohel Murshed and professor Viriato Semião for all the support and advices given during the realization of the master thesis.

I want also to thank greatly to Dr. Vânia Silvério for the valuable knowledge shared to me about microfabrication techniques and good engineering practices.

I also want to thank everyone who contributed direct or indirectly to this work, probably too many people that I cant mention all.

Last but not least, I must thank my friends, family and my girlfriend, who accompanied me in this great journey from the beginning to the end and were always there for me.

Resumo

A geração de microgotas num ambiente altamente controlável, como os canais microfluídicos, tem sido amplamente estudada nas últimas décadas devido à sua extensa gama de aplicações. No entanto, a sua dinâmica não é totalmente compreendida e a aplicação de nanofluidos na sua formação não tem recebido muita atenção. Neste âmbito, duas geometrias em T foram fabricadas em polidimetilsiloxano, usando métodos de litografia suave, com diferentes razões de aspecto de 0.335 e 0.176, e igual razão de largura de 1, para serem testados. As imagens das experiências foram obtidas com uma câmara CMOS monocromática, montada num microscópio. O processo de formação de microgotas foi caracterizado para os regimes de *squeezing*, transição e *dripping*, com uma fase contínua de óleo mineral com 1% em massa de Span 80 e uma fase dispersa de água destilada, para números Capilares entre 0.002 e 0.3 e razão de caudais entre 0.01 e 0.8. Verificou-se que o volume adimensionalizado aumentou com a razão de caudais e razão de aspecto, mas diminuiu com o número Capilar. Um ajuste linear verificou-se adequado para o regime de *squeezing* e um comportamento de potência para o regime de *dripping*. De seguida, foi estudada a adição de diferentes concentrações de nanopartículas de Al_2O_3 (0.01%, 0.025% e 0.1%) à água destilada. O volume adimensionalizado da gota aumentou com a concentração de nanopartículas para o regime transição, mas não se alterou significativamente para o regime de *dripping*. Isto foi atribuído à mudança nas propriedades físicas, especificamente um aumento na tensão interfacial e viscosidade.

Palavras-chave: Microfluidica, Microcanais-T, Nanofluidos, Microfabrico, Microgotas

Abstract

The generation of microdroplets in a highly controllable environment such as microfluidic channels has been widely studied in the last decades due to its large interdisciplinary range of applications. However, its dynamics are not fully understood and the application of nanofluids into droplet formation has not received much attention. Within this scope, two different T-shaped channels were fabricated in polydimethylsiloxane using soft lithography methods, with different aspect ratios of 0.335 and 0.176, and equal width ratio of 1, to be tested. The images of the experiments were acquired with a monochromatic CMOS camera, mounted on a microscope. The droplet formation process was characterized for the squeezing, transitional and dripping regimes, with a continuous phase of mineral oil with 1$\%$ w/w Span 80 and a dispersed phase of distilled water with w/w 0.05$\%$ fluorescent dye for Capillary numbers between 0.002 and 0.3 and flowrate ratios between 0.01 and 0.8. It was verified that the non-dimensional droplet volume increased with the flowrate ratio and aspect ratio but decreased with the Capillary number. A linear fitting was found appropriate for the squeezing regime, whereas a power-law behaviour adopted in dripping regime. Then, the addition of different concentrations of Al_2O_3 (0.01%, 0.025% and 0.1%) nanoparticles to the distilled water was studied. The droplet non-dimensional volume increased with the concentration of nanoparticles for the transitional regime but did not change significantly for the dripping regime. This was attributed to a change in the base fluid properties, specifically an increase in interfacial tension and viscosity.

Keywords: Microfluidics, T-junction, Nanofluids, Microfabrication, Microdroplets

Contents

List of Tables

List of Figures

Nomenclature

CMOS Complementary metal–oxide–semiconductor

DIW Distilled Water

IPA Isopropyl alcohol

MEMS Micro-electromechanical systems

PDMS Polydimethylsiloxane

PGMEA 1,2-Propanediol monomethyl ether acetate

PMMA Poly(methyl methacrylate)

SDS Sodium dodecyl sulfate

SEM Scanning electron microscope

w/w Weight on weight

Greek symbols

α Polydispersity index.

μ Molecular viscosity coefficient.

ρ Density.

σ Interfacial tension.

θ Static contact angle.

Roman symbols

Bo Bond number

Ca Capillary number

Re Reynolds number

We Weber number

Subscripts

av	Average.
c	Continuous phase.
d	Dispersed phase.
h	Hydraulic
max	Maximum.
ref	Reference condition.

Chapter 1

Introduction

1.1 Motivation

Since its advent, microfluidics has experienced an increase in its applications due to its inherent multidisciplinary character. Its advantages vary depending on the function, but the main characteristics consist in the miniaturization, specially in the chemistry and biological fields, where the amount of materials needed for a specific process decrease dramatically, giving unique advantages in terms of time and costs [1–3].

In 1982, with the development of MEMS (*Micro-eletromechanical systems*) and 8 years later through Manz et al. work [4], the field of μ-TAS(Micro total analysis systems) or Lab-on-a-Chip (LOC) devices was established. Commonly, microfluidic systems are combined with these portable LOC devices, integrating several functions of a regular laboratory test like sample transfer, mixing, heating, etc. in one single device [5].

One of the areas of microfluidics deals with 2-phase flows, when two immiscible fluids interact in such a way that droplets can be formed and manipulated in a precise manner. At the microscale, these blobs can have volumes down to the picoliter, granting faster phenomena such as mixing, reactions and high-throughput. It also allows several reactions to be performed at the same time in a parallel and serial circuit [2, 5].

The combination of droplet generation devices with daily life applications was first observed in the middle of the 20th century, with the ink-jet print technology [6]. This technology uses the fact that a liquid stream breaks into smaller drops under certain conditions, a phenomenon called Rayleigh-Plateau instability, owed to the extensive work performed by both authors on the subject [7].

These droplets have inumerous applications ranging from virus detection, fast analytical systems, development and screening of biological assays, the production of polymer particles, nanoparticles, in vitro compartmentalization and others [2, 8, 9]. Many operations such as droplet fission, fusion, sorting and mixing can be performed, allowing for a wide range of process possibilities [10], as shown in figure 1.1.

On the other hand, nanofluids are considered the fluids of the future. Although most of the focus of

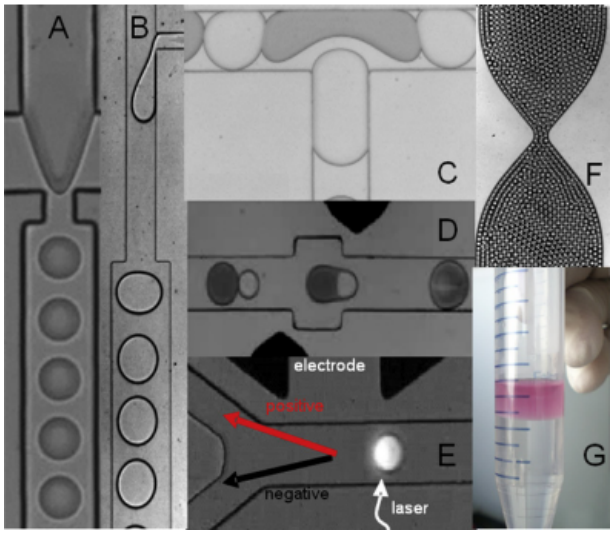

Figure 1.1: Droplet formation in a flow-focusing geometry (A) and T-junction (B) channels. Manipulation of the generated droplets can involve splitting (C), fusion (D), sorting (E) and incubation (F,G). Adapted from [11].

their research is based on their improvement of thermophysical properties related with heat transfer, it also has applications in MEMS and biotechnology, such as drug delivery in cancer therapy [12–14]. In fact, the addition of small particles to a base fluid can be traced back to Maxwell's theoretical work on the determination of solid-liquid suspensions effective thermal conductivity, in 1881. In between this date and 1995, a lot of experimental studies have been performed to this effect; however they were limited to micrometer sized particles. Only in 1995, the addition of truly nanoparticle dimensions, revolutionized this idea since problems like clogging, erosion and increased pressure drop were largely diminished [12]. With the current nanophase technology, it is now possible to have orders of magnitude of the 10^{th} of nanometer scale, with a typical length from 1-50 nm. A lot of challenges still need to be overcome to fully understand nanofluids behaviour and improve current and future applications.

Having this in mind, this work has the purpose to increase the understanding of droplet based microfluidics area, while presenting research data for future applications where the dispersed phase can involve nanofluid suspensions.

1.2 Topic Overview

1.2.1 Theoretical principles

Microfluidics is the subject of fluid mechanics area that deals with the study and applications of fluid flows at the microscale, where the conventional flow theory no longer applies accurately [3]. At these small scales, effects that were unimportant at macroscale appear and the boundary conditions influence the flow dynamics differently. The ability to contain and manipulate small volumetric amounts of fluid has many benefits in comparison with macrofluidics, mainly through the reduction of experimental quantities. It is useful to introduce the concept of scaling laws. In fact, flow scales are governed by the competition

of different phenomena, and the importance of some phenomena changes when reducing dimensions. When we apply this concept for microscales, we get [15]:

$$\frac{surface forces}{volume forces} \sim \frac{l^2}{l^3} = \frac{1}{l} \tag{1.1}$$

This means that when the length l is very small, such as in a microsystem, surface forces start to become more important than volumetric ones. That is the case for interfacial tension, which is crucial for two-phase flow behaviour. In this type of field, there exists an interface between two different immiscible fluids. This region of separation between two different materials that do not mix with each other appears due to the different physico-chemical properties and can be observed for fluids, solids and different phases.

Interfacial tension

Interfacial tension has a simple definiton of the energy that costs to increase the size of an interface between two fluids. This energy is related with the Gibbs free energy G (p,T,N):

$$\sigma \equiv \left(\frac{\partial G}{\partial A}\right)_{p,T,N}$$

where θ is the contact angle and σ (N/m) is the interfacial tension between fluids. Thermodinamically, this means that a certain system at certain conditions, in order to be in equilibrium such that its (free) energy is minimum, has to reduce the interfacial area. This property can also be explained physically, due to molecular bonding, bulk molecules have larger number bonding connections than surface molecules, as depicted in figure 1.2 for as gas-liquid free surface.

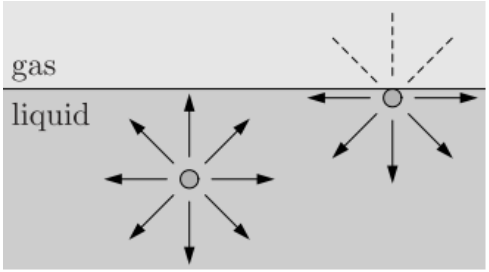

Figure 1.2: Intermolecular connections between liquid molecules in the presence of a surface. The net downward force at the surface is not 0 due to intermolecular attractive forces, resulting in a surface tension that minimizes surface area. Adapted from [15].

Having less bonding connections, surface molecules are in a higher energy state. This interaction minimizes free surface area due to presence of a downward force at the interface, which results from the existence of interfacial tension. Furthermore, when a droplet is at rest on top of a surface, it will adopt a surface curvature that will depend on the surface tension between the 3 phases:

$$\theta = cos^{-1}\left(\frac{\sigma_{sg} - \sigma_{sl}}{\sigma_{lg}}\right) \tag{1.2}$$

with σ_{sl}, σ_{lg} and σ_{sg} are the solid-liquid, liquid-gas and solid-gas interfacial tensions. This is called Young's equation and it represents the force balance in the horizontal direction, which is also applicable

to liquid-liquid phases when both are immiscible. According to the liquid curvature θ, the surfaces can be characterized differently. If $\theta < 90°$, the droplet is said to be *wetting* the surface, whereas if $\theta > 90°$ the droplet is *non-wetting* the surface. When a liquid can wet the surface, the surface is hydrophilic, and its hydrophobic when the opposite is true. This has implications in flow behaviour and droplet formation process, at it can be seen on figure 1.3 (a,b). In order to achieve the formation of a droplet of a certain fluid, that particular fluid has to non-wet the surface. This property can be evaluated by performing a sessile drop test, seen in figure 1.3 (c,d), where the static contact angle θ from equation 1.2 is measured.

(a) Segmented flow (hydrophilic surface)

(b) Droplet based microfluidics (hydrophobic surface)

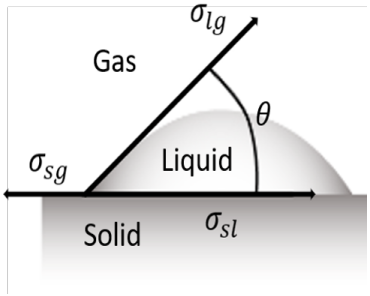

(c) Typical triple contact line observed in a hydrophobic free surface.

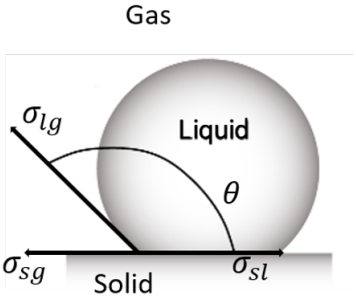

(d) Typical triple contact line observed in a hydrophilical free surface.

Figure 1.3: Schematics of different patterns observed depending on the wettability of surfaces. The contact angle θ will depend on the solid-liquid (σ_{sl}), liquid-gas (σ_{lg}) and solid-gas (σ_{sg}) interfacial tensions. Adapted from [2].

One of the consequences of the interfacial tension is the existence of a pressure difference across any curved interface. This is given by Young-Laplace pressure equation which states that $\Delta p = \sigma \left(\frac{1}{R_1} + \frac{1}{R_2} \right)$, where R_1 and R_2 are the two radii of the interface, as schematized in figure 1.4 [3, 15].

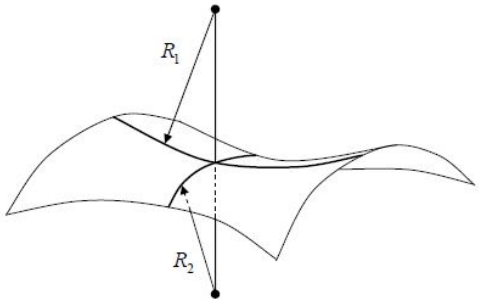

Figure 1.4: Principal radii of curvature R_1 and R_2 associated with an interface, at a specific point [16].

Without this property, emulsification techniques would not be possible since immiscible fluids would just flow along side without forming droplets or bubbles. This will be discussed more in-depth in the

subsection 1.2.2.

Relevant dimensionless numbers for microdroplets formation

The most used dimensionless number for fluid dynamics is the Reynolds number (Re):

$$Re = \frac{\rho V L}{\mu} \tag{1.3}$$

where ρ is the fluid density, V is the average velocity of the fluid, L is a characteristic length and μ is dynamic viscosity.

Physically, Re represents the balance between inertia forces and viscous forces and it evaluates if a flow is in laminar or turbulent regime. In laminar regime at low Reynolds number, the flow is smooth and steady and it is the case for most microfuidic devices and droplet generators [3, 15, 17]. Interestingly, the formation of droplets actually arises from non-linearities and irregular pattern formations introduced by the geometry, to be explained later. In typical droplet formation studies, inertial effects are neglected since the flowrates used are low and the characteristic lengths are of the order of 1-100 μm, so Re range from 10^{-6} to 1.

Additionally, another very important parameter for droplets and their characteristics is the Capillary number (Ca), which represents the ratio between viscous forces and interfacial tension forces:

$$Ca = \frac{\mu V}{\sigma} \tag{1.4}$$

where σ is the interfacial tension between both fluids. This parameter is critical since it combines most of the relevant properties for droplet formation and, as it will be seen, it defines different droplet formation regimes.

For multi-phase flows, the Weber (We) number is an important parameter, which is defined as We = $\frac{\rho V^2 D_H}{\sigma}$, where D_h is the hydraulic diameter of the channel used. It compares the inertia of a fluid with the interfacial tension and, since it scales by the power of 2 with velocity, it is typically verified that We$<$1 for low-speed applications. The Bond number (Bo), defined as Bo = $\frac{\Delta\rho g D_H^2}{\sigma}$, where $\Delta\rho$ is the density difference between both fluids, is also relevant in certain microfluidic applications such as the generation of droplets when the wetting fluid is a gas. It compares gravity effects with interfacial tension and, for liquid-liquid droplet generation, the density difference term $\Delta\rho$ is normally so low that buoyancy effects are negligible.

For the case of the droplet generation, since there are two different immiscible fluids interacting, the choice of which fluid properties to use is not evident. The values from the continuous phase fluid are largely used as the defining controlling parameters [18, 19].

Internal flows

For internal flows, the characteristic length for circular cross-section channels is the diameter. However, for non-circular cross section cylinders, as it is the case for most of microfluidic devices, an hydraulic diameter is used to calculate the dimensionless numbers. It is based on the width, height and shape of the cross section [17]:

$$D_h = \frac{4A}{P_{wet}} \tag{1.5}$$

where P_{wet} is the wetted perimeter of the cross section and A is the cross-sectional area. For a rectangular duct fully filled, this reduces to $D_h = \frac{2Wh}{W+h}$, where h and W are the height and width of the cross-section, respectively.

1.2.2 Droplet based microfluidics

Emulsions are present in our daily life and most of them are manufactured, such are the examples of yoghurt and cheese. They consist of a mixture of two or more liquids that are usually immiscible, such as oil and water, and can be formed by shearing. They are used in many industrial applications like food, cosmetics, pharmaceuticals, painting and many others [20].

Although emulsifying techniques have been around for a long time, bulk methods do not offer reproducible and controllable pattern formations. Most microdroplet generation systems are able to form monodisperse droplet sizes with polydispersity as low as 2 $\%$ [2]. Polydispersity is a mathematical expression for the droplet size deviations from the mean values, and is defined by the following equation:

$$\alpha = \frac{\delta}{d_{av}} \times 100\% \tag{1.6}$$

where α is the polydispersity index, d_{av} is the average droplet dimensions in study (can be diameter or volume) and δ pis the standard deviation of the distribution.

The first production of monodisperse droplets in a microfluidic T-junction was reported by Thorsen et al. [21]. They attributed the formation of droplets to a competition of shear and interfacial tension stresses:

$$r \sim \frac{\sigma}{\mu\dot{\varepsilon}} \tag{1.7}$$

where r is the droplet radius, and $\dot{\varepsilon}$ is the shear rate. Since then, a lot more methods have been discovered and studied. They can be divided in two types: active and passive. Droplet generation can be forced by active methods like eletric fields, piezoeletric actuators and other external driving forces [9, 19]. Oppositely, passive methods do not need any driving forces, droplets are formed mainly due to geometry and by tuning kinematic and physical properties of the fluids. The interface between both immiscible fluids is subjected to natural forces arising from the geometry, that create instability, non-linearity and induces droplet break-up. Some of the geometries used for droplet generation are schematically presented in figure 1.5.

Although passive methods are always preferable, active methods do offer a more controllable and defined droplet formation, often required for LOC applications, for example [2, 18].

Generally, it is observed that the droplet formation(size/polydispersity) process depends on [2]:

- Flow rates of both fluids;

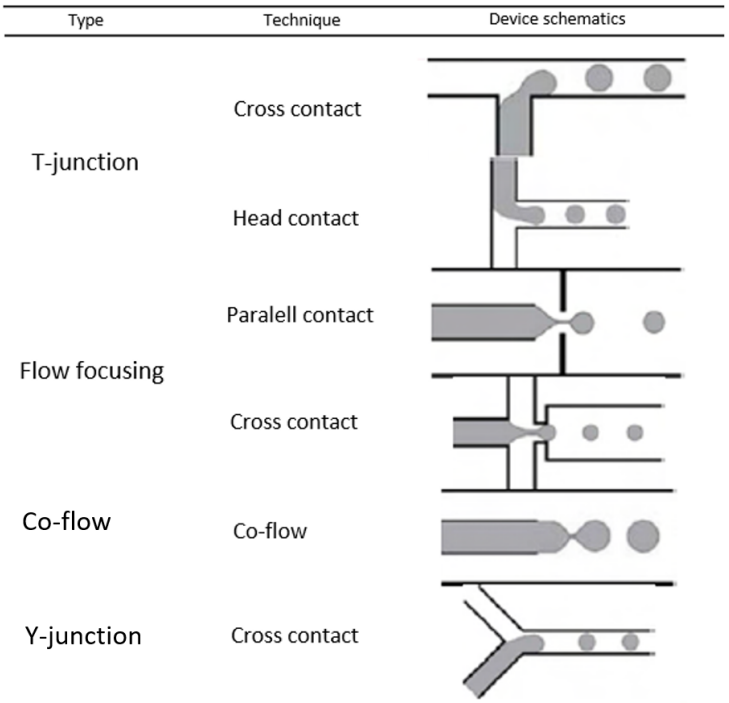

Figure 1.5: Characteristics of typical PDMS microfluidic droplet generator devices. Adapted from [9].

- Channel dimensions;
- Viscosities of both fluids;
- Interfacial tension between both fluids (presence and concentration of surfactants);
- Wettability of channel walls.

The effects from these parameters are slightly different depending on the generation mechanism used and the droplet formation regime. This review focuses on T-junction geometries since this geometry is used in the experimental part of the work.

Droplet generators: T-junctions

As it was said before, T-junctions are one of the most common techniques to achieve reproducible and controllable droplet formation, and its mechanisms have been widely studied experimentally [22–30] and numerically [31–36].

In these types of cross-contact geometries, the two immiscible fluids interact at the intersection between the two inlet channels, where the local velocity field, determined by the geometry of the junction and the flow rates, deforms the interface. Eventually droplets pinch off from the dispersed phase thread by instability [1], as depicted in figure 1.6. With this design, its possible to have 3 different droplet generation processes depending on the chosen fluid channels. Besides the ones represented in the figure, another route was sucessfully tested by Xu et al. [37], using a capillary tube for the continuous phase channel. In their method, the continuous phase interrupts the dispersed phase flow, blocking and force it to break into droplets.

Its common to non-dimensionalize geometrical dimensions of a T-shaped microchannel, depicted in figure 1.7, and define the width ratio Λ and aspect ratio Γ:

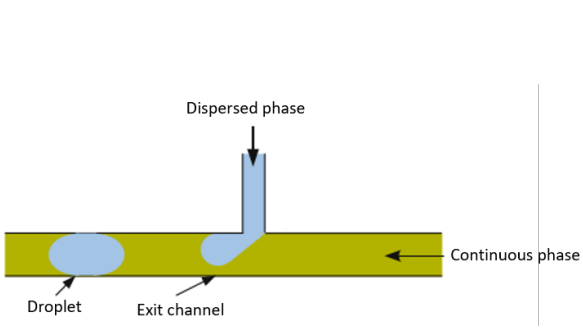

(a) T-junction with cross contact droplet formation.

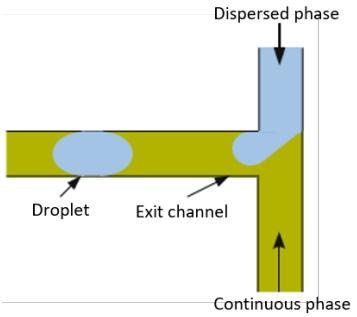

(b) T-junction with head contact droplet formation.

Figure 1.6: Schematic of T-shaped microchannels for droplet based microfluidics where the dispersed and continuous phase meet at a 90° junction. Adapted from [35].

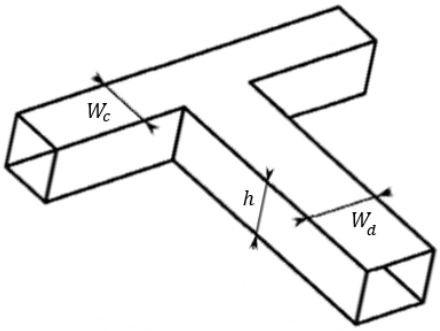

Figure 1.7: Designed dimensions for a T-shaped microchannel. In this case, the width of the main channel W_c is constant. Adapted from [38].

$$\Lambda = \frac{W_d}{W_c} \tag{1.8}$$

$$\Gamma = \frac{h}{W_c} \tag{1.9}$$

W_c and W_d are the widths of the continuous and dispersed phase channels, respectively. The droplet volume or diameter is also typically made non-dimensional, either as d'= $\frac{d}{W_c}$ and V'= $\frac{v}{W_c^2 h}$, where v is the droplet volume and h is the height of the microchannel (that is usually constant due to manufacturing constraints) [23, 26, 27]. These dimensions influence droplet formation since they are related with important process parameters, like fluid flow rates, that directly influences Ca. Furthermore, the blockage of the main channel due to the protruding dispersed phase, inherently related with a confinement imposed by the cross section area, is also relevant in some droplet formation regimes, as it will be discussed. Remaining dimensionless groups include flow property ratios such as the flow rate ratio Q=$\frac{Q_d}{Q_c}$, the viscosity ratio $\lambda = \frac{\mu_d}{\mu_c}$ and the density ratio $\rho = \frac{\rho_d}{\rho_c}$ and dimensionless numbers such as Capillarity numbers $\text{Ca}_c = \frac{\mu_c V_c}{\sigma_c}$, $\text{Ca}_d = \frac{\mu_d V_d}{\sigma_d}$ and Reynolds numbers $\text{Re}_c = \frac{\rho_c V_c D_H}{\mu_c}$, $\text{Re}_d = \frac{\rho_d V_d D_H}{\mu_d}$. Typically, the density ratio is not considered in the analysis since for liquid-liquid phase flows, the pressure difference between these is negligible.

Droplet formation regimes in T-shaped channels

According to De Menech et al. [31], 3 different regimes of droplet formation are commonly observed, depending on the continuous phase Ca: squeezing, dripping and jetting. Some authors also include a transitional regime between squeezing and dripping [27], but this is somehow controversial. Regime identification is somewhat dependent on the author's subjectivity since unique characterizing parameters are not completely established. Since the continuous phase Ca (Ca_c) is the most important parameter in the identification of droplet formation regimes, it is usually used without any subscript. This notation will be adopted throughout the thesis and emphasized in the beginning of each chapter.

In a T-junction microchannel, droplet formation is broadly segmented in three steps: (i) the flow of continuous and dispersed phase meet at the junction, leading to the appearance of well defined interface; (ii) the interface will grow into the main channel due to injection of dispersed fluid and deform; (iii) droplets are pinched off and carried in the main channel by the continuous phase fluid.

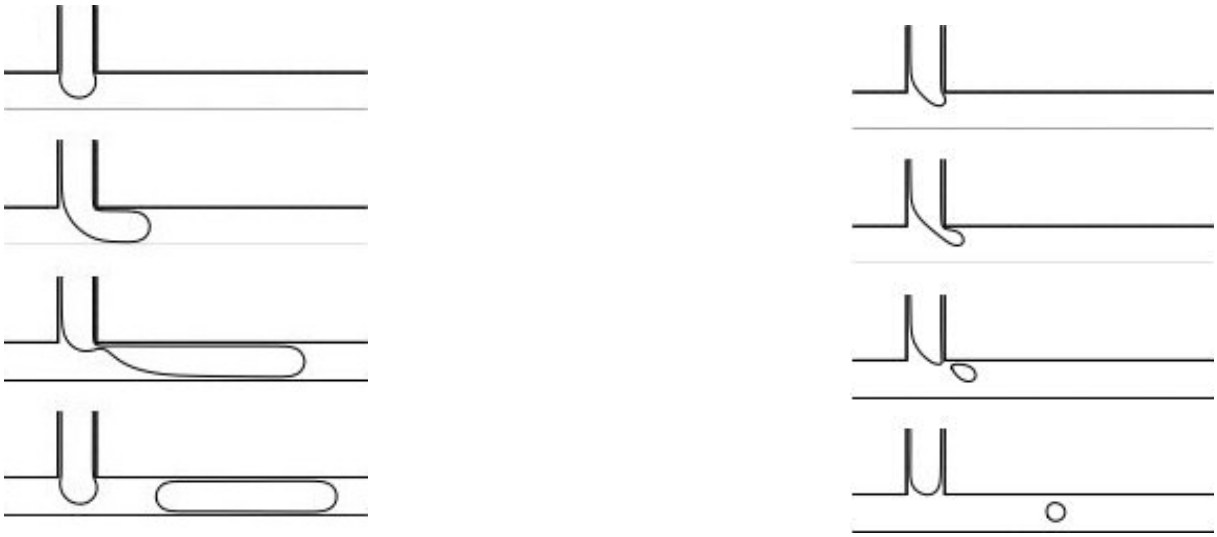

(a) Squeezing regime

(b) Dripping regime.

Figure 1.8: CFD simulation snapshots for the squeezing and dripping regimes at: (a) Ca =0.00056, Q_d = 0.004; (b) Ca =0.059, Q_d = 0.008. Adapted from [32].

Squeezing regime is characterized by low Ca numbers, typically Ca $< 10^{-2}$ [22], where droplet detachment is dominated by a dramatic increase in pressure force upstream of the forming interface. The shear force is not strong enough to cause relevant deformation and the formed thread will grow and obstruct the channel, restricting the continuous phase flow. As the Ca number is increased, the dripping regime is attained where the shear forces exerted by the continuous phase start to play an important role in droplet formation, deforming the interface as it enters the junction. The deformation forces become high enough ensuring droplets are detached before even filling the entire channel. Once the dispersed phase thread reaches a critical size, the interfacial tension force is not strong enough to resist the elongation and the droplet detaches. Both the squeezing and dripping regimes are illustrated in figure 1.8 for a T-junction microchannel, where the physical description given above is schematically shown. It was further observed that, increasing Ca in the dripping regime, dislocates the formation zone downstream of the exit channel and away from the junction. The formation enters the jetting regime,

when there is a clear development of an elongated finger, and droplet detachment occurs at the end of the jet by Rayleigh-Plateau instability. Finally, for Ca numbers large enough, paralell flow is observed and both fluids flow smoothly with a well paralelly defined interface and no droplet formation occurs. Between the squeezing and dripping regimes, it appears an intermediate regime where both shear and pressure forces share similar importance in the process, which is known as the transitional regime [23, 24, 27].

Parameters influencing droplet formation

Droplet size can be controlled by numerous parameters, arising from microchannel design and fluid and flow properties.

In order to accomplish a water-in-oil droplet formation, its very important to assure an hydrophobic surface of the microchannel walls meaning that the continuous phase (in this case, oil) should wet the channel surface favorably [1]. Elastomers like PDMS (Polydimethylsiloxane) are naturally hydrophobic whereas silica and glass are hydrophilic. Nevertheless, various methods can be used that render a surface to switch wettability properties, permanent and non-permanent, and also surfactants can be added to the fluids [2, 19]. Surfactant addition repercussions are dependent on its concentration and type (*i.e.* liquid-surfactant pairing), and it has a stabilizing effect on the liquid-liquid interface by lowering the interfacial tension while preventing coalescence [2, 20, 39]. The latter is specially important in microfluidic applications requiring droplet manipulation.

Surfactants are amphiphilic molecules that posess both an hydrophilic and hydrophobic part, as shown in figure 1.9 (a). They actuate by adsorbing at the two-phase interface, with their polar heads in the water phase and their tails in the oil phase [20], and by self-agglomeration in molecular clusters, called micelles, in a saturated solution [39].

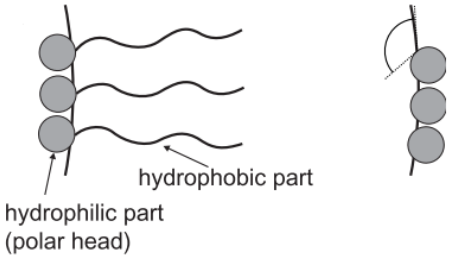

(a) Schematic of a molecular surfactant having a polar head and a hydrophobic tail. Adapted from [2].

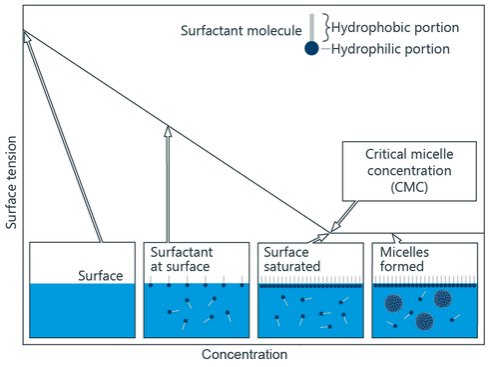

(b) Surface tension variation with the concentration of surfactant in the solution (Credits: Krussscientific).

Figure 1.9: Schematic of a molecular surfactant and functioning mechanism of the addition of surfactants in a liquid solution.

Several studies show that, before the critical micelle concentration (CMC) is reached, there is a decreasing effect on the interfacial tension and droplet diameter with the increase in surfactant concentration, as seen in figure 1.9 (b) [20, 40]. Wang et al. [40] verified that the generated droplets become smaller as the surfactant concentration increases and that surfactant dynamics has a strong impact on droplet formation. Therefore, material selection and surface wetting properties are crucial for microfluidics droplet applications.

The microchannel geometry and dimensions also affect the droplet formation process, either by confinement, either by influencing other parameters. The non-dimensional droplet diameter d' is observed to increase with the aspect ratio Γ [23, 34] and width ratio Λ [33, 41], either by increasing the depth h, decreasing the continuous phase width W_c or increasing the dispersed phase width W_d.

From the variables present in the Ca number, it is known that droplet formation is affected by changing viscosity (μ), interfacial tension (σ) and velocity (V) of both phases.

Altering the flowrates of both phases affects droplet formation by introducing shear forces tangent to the interface that are responsible for its deformation and subsequent break-up. Droplet size is observed to increase as the flow rate ratio Q increases but becomes smaller as Ca increases. In the squeezing regime, literature shows that the flowrate ratio Q is a dominant parameter defining droplet size to increase linearly with it. Garstecki et al. [22] data shows this trend for $Q > 1$, but also verifies that it is independent of Q for very low flowrate ratios, where the length of the droplets reached an assymptotic limit, as it can be seen in figure 1.10. This was attributed to high confinement conditions obtained from the geometry. In the dripping regime since the Ca is higher, droplet formation is less dependent on the flowrate ratio. Moreover, numerical data from De Menech et al. [31] shows that the effect of confinement still play a role in defining droplet formation, specially if the formed droplet sizes introduce non negligible continuous phase flow restriction.

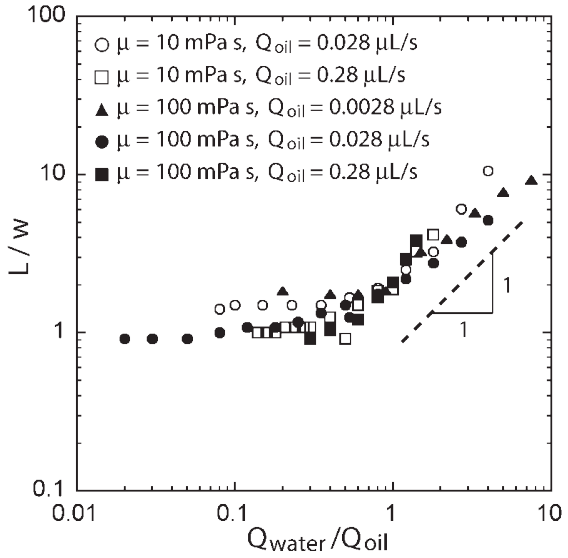

Figure 1.10: Variation of the droplet length with Ca at dispersed phase flow rates Q_d of 0.0028, 0.028 and 0.28 μL/s [22], for two different viscosity ratios.

In the dripping regime, droplet size is more influenced by Q_c, i.e., Ca, than from the flowrate ratio Q. Figure 1.11 shows that droplet diameter decreases with Ca and hardly changes with Q_d for the same Ca conditions [32]. It is also observed that droplet size does not vary significantly for higher Ca in the dripping regime [33].

In water-in-oil emulsions, altering viscosity can be done by changing oil types, mixing water with other solutions or compounds, changing temperature, and others [23, 42–44].

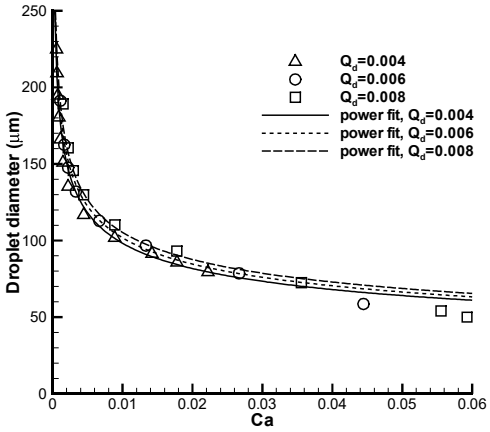

(a) Variation of the droplet diameter with Ca at dispersed phase flow rates Q_d of 0.004, 0.006 and 0.008 [32].

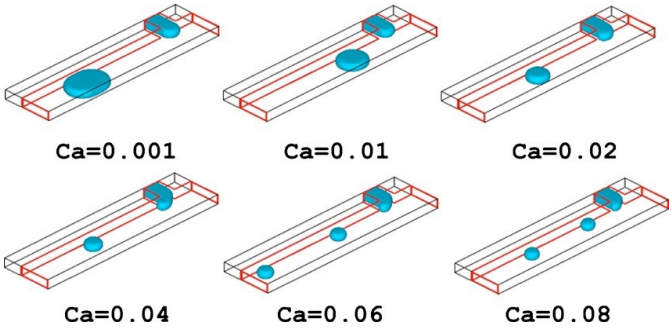

(b) Droplet size for the squeezing to dripping regime for a flowrate ratio of Q=1/20, λ=1/2, and Γ = 1/3 [33].

Figure 1.11: Variation of the droplet size as a function of Ca obtained from literature.

In the squeezing regime, droplet formation is verified to be independent of the viscosity ratio λ, as it does not depend significantly on the shear forces [23, 32]. In the dripping regime, its effect starts to become noticeable and it shows to have a decreasing effect on droplet size [32].

Both viscosity and interfacial tension, which play an important role in droplet formation, are temperature dependent. Murshed and Nguyen [45] explored nanofluids and temperature dependence in droplet generation devices. The introduction of nanoparticles in the dispersed phase of a T-junction, directly affects the process by introducing a small change in viscosity and a large decrease in interfacial tension, as shown in figure 1.12 [42, 43]. Moreover, those authors argued that the change in properties was insufficient to explain some of the droplets behaviour and that nanoparticles can agglomerate during the tests, which can cause property changes during the process.

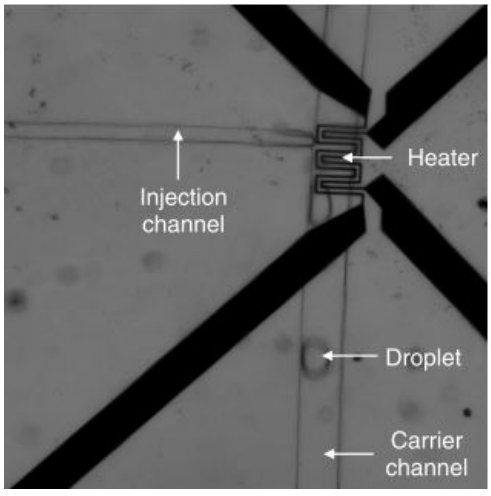

(a) Experimental setup of a T-junction with integrated microheater and temperature sensor.

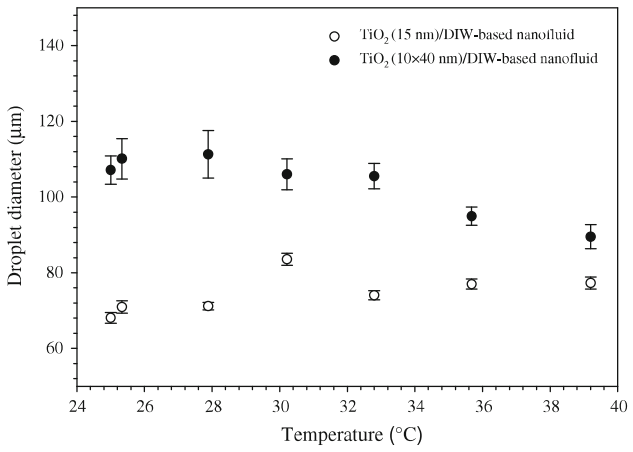

(b) Variation of droplet size with temperature for 2 different types of nanoparticles in a T-junction (h = 30 μm, W_c = 100 μm and W_d = 50 μm).

Figure 1.12: Influence of the addition of TiO_2 nanoparticles in a T-shaped heated droplet generator [43].

The preparation of nanofluids is usually done in a two-step process, obtaining them commercially,

and mixing it afterwards with the base fluid. This method has the drawbacks of the particles not always having the exact dimensions labeled by the supplier and forming clusters, as they quickly agglomerate inside the containers due to their high surface energy and strong attractive forces. Due to this drawbacks, an effective way of mixing and declustering is needed. This is usually achieved using a mechanical stirrer and ultrasounds, or high shear homogenizers. [46]. On the other hand, in single-step process, the synthesis and dispersion of nanoparticles in the base fluid are done simultaneously. This method provides a more stable and disperse nanofluid, but it is more expensive, slow and with a limited quantity of production. Longer stability times are required for most nanofluid applications and it depends on both the base fluid-nanoparticles pairing, but, for research purposes, the two-step method is more feasible.

Scaling laws

Different models which predict droplet size based on its influential parameters are going to be approached in this subsection. As outlined, numerous factors influence droplet formation and in diverse ways, depending on the regime at study. Regardless, it is important for practical applications to be able to make this kind of predictions for a specific set of conditions.

Considering a 2-stage process of growth and neck squeezing, and arguing negligible influence of Ca on droplet size in the squeezing regime, Garstecki et al. [22] proposed a scaling law based on a linear fitting between droplet length L and Q:

$$\frac{L}{W_c} = 1 + \frac{d_{neck}}{W_c} \times Q \tag{1.10}$$

where d_{neck} is the forming droplet neck diameter. The authors observed that in this regime, the final thread length that blocked the main channel was almost equal to the width of the main channel W_c and its rate of growth was proportional to Q_d. Then, the thread neck, assumed to be equal to W_d, was squeezed due to the increase of pressure upstream, proportional to Q_c. However, the model was found to be limited to the experimental conditions from their work ($\Lambda < 0.5$, $h < W_c$ and $Ca < 0.01$). This scaling was further adapted to include a broader range of geometries, by replacing both coefficients by appropriate fitting parameters that depend on the T-junction dimensions [24]. This was found to properly relate purely squeezing conditions and indicate that this regime is mainly governed by Q and T-junction geometry.

For the transitional regime, Christopher et al. [23] deduced a system of 2 equations to determine droplet volume, based on a force balance between squeezing pressure, interfacial tension and shear force:

$$V' = \left(\frac{b}{W_c}\right)^2 + \Lambda Q \tag{1.11}$$

where V' is the droplet volume, adimensionalized by $W_c^2 h$, and b is the length of the emerging thread at break-up, which is unknown and a function of the Ca. This model was observed to be accurate for low Ca and $\lambda \approx 1$, but failed remarkably for higher Ca and different λ. Moreover, they discovered that for low viscosity ratios λ, the non-dimensional length L exhibited a power-law dependence on Ca, that was independent on the flowrate ratio. Later, Liu and Zhang [41] generalized this model to also consider the

flowrate ratio Q effect:

$$\frac{L}{W_c} = (\varepsilon + KQ) \times Ca^m \tag{1.12}$$

where ε, K and m are fitting parameters.

Other correlations based on force balances, step models and theoretical analysis have been proposed in literature [26, 27, 47], yet they are not able to predict accurately results from other researchers.

1.3 Contribution and objectives

Considering the bibliographic review done in the previous sections, the study of formation and manipulation of monodisperse droplets in microfluidic devices, specially T-junction, has been widely studied experimentally [22–30] and numerically [31–36]. Despite all these efforts, the mechanisms that control this process and the effects of important parameters for droplet formation seem not to be yet fully comprehended.

There is a promissing future in nanofluid applications in microfluidics and droplet generators, since these particles are several orders of magnitude smaller than the typical microchannel dimensions, which avoids clogging problems, for example. Research towards the employment of these as the dispersed phase fluid has not received much attention, since the works of Murshed et al. [42, 43]. Due to this fact, there is lack of data in the use of nanofluids in microchannels for droplet-based applications.

It is crucial to have a solid knowledge supported by a vast collection of experimental data, that contributes to a deeper understanding of the phenomena. This work aims to complement the current knowledge in droplet formation dynamics, by providing data in innovative experimental conditions. Furthermore, the application of Aluminium Dioxide Al_2O_3 nanoparticles in a T-shaped droplet generator was never studied until this work, including the effects of nanoparticle concentration in the droplet size.

In this context, an experimental study on the formation of distilled water and aqueous Al_2O_3 nanofluid microdroplets in a microfluidic T-junction channel will be performed. The methodology relies upon a process visualization in a optical microscope connected to a CMOS camera and digital image post-processing. For this purpose, two different geometries were fabricated by soft lithography methods in order to assess the geometrical effect on this process, namely the aspect ratio Γ, while keeping the width ratio Λ between the dispersed and continuous phase segments. The effects of controlling parameters on droplet size and formation times will be studied. These parameters include the flowrate ratio Q, Capillary number of the continuous phase Ca and nanoparticle concentration. The outcome originated in the identification of different droplet formation regimes in which these parameters affected distinctively droplet generation process. After analysis of the mechanisms involved in each regime, the results obtained for the distilled water were compared to the ones acquired for nanofluid.

1.4 Thesis Outline

This thesis is divided into 5 chapters:

In the first chapter(Introduction), a brief review of the literature about the subject is done, pointing the motivations, objectives of the work and contributions that were intended.

In the second chapter(Experimental Work), a detailed explanation of the experimental work is presented, including the fabrication process, materials and equipments used and the acquision of images.

In the third chapter(Digital image processing), a detailed overview of the image treatment, analysis and droplet diameter calculation processes is given.

In the fourth chapter(Presentation and Discussion of the Results), the results obtained are presented and discussed, having in mind the objectives delineated in the first chapter.

In the last chapter(Conclusions and Future Work), the conclusions from the work are exposed and the proposes for future work are given.

Chapter 2

Experimental Work

The experimental work developed for this thesis encompasses both the fabrication process of the T-junction microchannels, and all the preparation and testing performed in these. The device fabrication steps were done at (INESC - Microsystems and Nanotechnologies) Lisbon facilities.

2.1 Equipments

In this section, a brief description of the equipments used is provided, both for the microfabrication processes and for the experimental tests. The technical characterization was supported by the manufacturer's manual. This section needs to be closely linked to the experimental procedures, which will be discussed in section 2.2 .

2.1.1 Vertical laminar flow station

Some microfabrication steps can be compromised if a clean environment is not ensured in the working table/equipments, specially before applying the photoresist layer on top of the wafer. For this matter, a vertical laminar flow station is used as it incorporates HEPA/ULPA integrated fan/filter modules that remove unwanted particles to meet cleanliness requirements of ISO5 standards.

2.1.2 Spin coater

Photoresist application is done by a process called spin coating, performed by a spin coater. This certifies a uniformly spread layer on the surface, since any thickness variations can cause problems during developing and subsequent resist removal. The wafer is held on a vacuum chuck and a rotation motion provides a centrifugal force on the photoresist. The resist thickness obtained from this equipment will depend on the amount of resist dispensed, the spin speed, viscosity, surface tension, and drying characteristics (solvent dependent) [3]. The spin coater used is the *WS-650-23NPP* from *Laurell Technologies*. This equipment and others used are present in the figure 2.1.

Figure 2.1: Equipments used in the Soft Lithograpy Laboratory at INESC-MN facilities during SU-8 mold and PDMS membrane fabrication.

2.1.3 Profilometer

During the soft lithography process, it is important to check the resist thickness and features size and shape, after the SU-8 mold is done, to assure the correct dimensions of the channels. To the first objective, a profilemeter such as the *Alpha Step 200* from *Tencor*, shown in figure 2.2 (a), can be used.

This model can characterize the surface profile by means of a conical stylus, ideal to measure film thicknesses and roughness of the mold. The technical specifications are displayed in table 2.1.

Table 2.1: Profilometer technical specifications

Characteristic	Value
Vertical resolution	5 Å (kÅ range), 5 nm (μm range)
Horizontal resolution	400Å
Stylus	Standard 12.5 μm radius
Vertical range	±160 Å (kÅ range), ±160 μm (μm range)

2.1.4 Analytical balance

In order to ensure the right proportions of PDMS polymer and curing agent during the microfabrication, measure densities and to have the correct volume % of nanoparticles in the aqueous nanofluid, an analytical balance is required. For nanofluid preparation, the model *ABS 80-4N* from *Kern*, figure 2.2

(a) Measurement of SU-8 resist thickness using the *Tencor Alpha Step 200*.

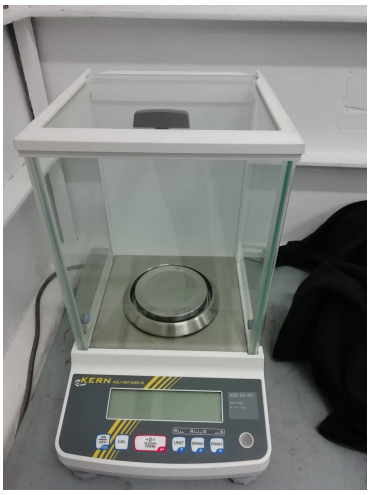

(b) Model *ABS 80-4N* analytical balance from *Kern*.

(c) *LVDV-II+Pro* viscometer from *Brookfields Engineering*.

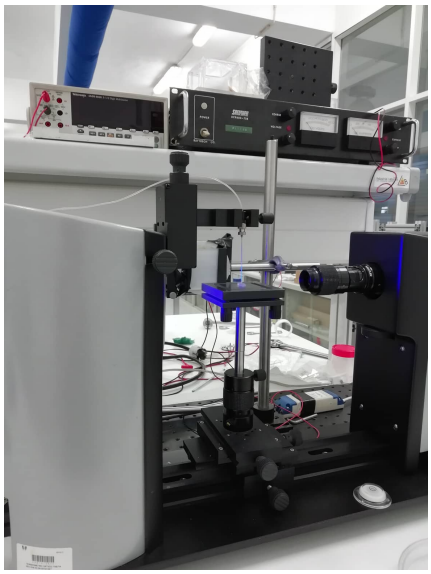

(d) Optical tensiometer *Theta* from *Attension*.

Figure 2.2: Some equipments used during the experimental work.

(b), was used, where the samples were poured into a 150 mL beaker. The technical specifications of the balance are listed in table 2.2.

Table 2.2: Analytical balance technical specifications

Characteristic	Value
Maximum capacity	82 g
Readability	0.1 g
Repeatability	0.2 g

2.1.5 Viscometer

In order to determine the viscosity of the working fluids, the *LVDV-II+Pro* set from *Brookfields Engineering* viscometer on figure 2.2 (c) was used. This viscometer works by means of conical spindle rotation, a static plate where the fluid stands on and by measuring shear rates and shear stresses resulting from the applied forces. For the operation, a 0.5 mL fluid sample is poured into a cilindrical chamber and the spindle is rotated at varying rotation speeds. This equipment is connected to a computer, where *Rheocalc* software records the shear rate values and calculates the values of shear stress with the torque applied by the fluid to the spring system of the viscometer.

In the table 2.3, technical specifications of this equipment are displayed.

Table 2.3: viscometer and spindle technical specifications.

Characteristic	Value
Rotational speed	0.1 - 200 rpm
Dynamic viscosity	0.15 - 3065 cP
Measurement precision	$\pm 1.0\%$ of full scale range
Viscosity Repeatability	$\pm 0.2\%$ of full scale range

2.1.6 Optical tensiometer

Another important equipment for the working fluids properties characterization, namely for the determination of the interfacial tension between the dispersed and continuous phases, is the optical tensiometer *Theta* from *Attension*. This equipment is composed by a video camera, an adjustable sample stage, a LED light source and a picoliter dispenser, as shown in figure 2.2 (d). With this setup, a variety of measuring experiments can be performed, including the sessile drop and pendant drop methods.

2.1.7 Ultrasonic homogenizer

The most common method for declustering of nanoparticles is by ultrasonication. For this work, the equipment used was the UP200Ht from *Hielscher Ultrasonics*. The handheld ultrasonic processor was mounted in a protection box so the system is stationary while in use and also allowing the control of the probe depth, as shown in figure 2.3 (a). This device generates ultrasonic waves in the liquid suspension by means of a sonotrode, inducing cavitation and mechanical vibration of the particles. Being a direct method, its energy output is bigger than in an ultrasonic bath, for example, being preferable to disperse the nanoparticle powder within the distilled water (DIW) [48]. The nanofluid samples were sonicated at a an amplitude of 60 $\%$ and at a frequency of 26 kHz, in continuous mode operation. The sample was not sonicated for a long time due to bulk heating of the nanofluid that can lead to evaporation and consequent errors in the $\%$ concentrations. The samples were inspected visually for good dispersion. This was enough since stability was only needed for the sufficient time to run the experiments. The technical specifications of this equipment are shown in table 2.4.

Table 2.4: UP200Ht handheld ultrasonic homogenizer technical specifications

Characteristic	Value
Working frequency	26 kHz
Control range	$\pm$ 1 kHz
Efficiency	$> 90\%$
Nominal power	200 W

2.1.8 Magnetic stirrer

Before the disruption of nanoparticle clusters, it is important to ensure that an homogenized dispersion is obtained. To this purpose, a magnetic stirrer was used, more specifically the *Rotilabo MH15* heating magnetic stirrer from *Carl Roth Gmbh*, displayed in figure 2.3 (b). The technical specifications of the magnetic stirrer can be found in table 2.5.

(a) UP200Ht handheld ultrasonic homogenizer from *Hierschel Ultrasonics*.

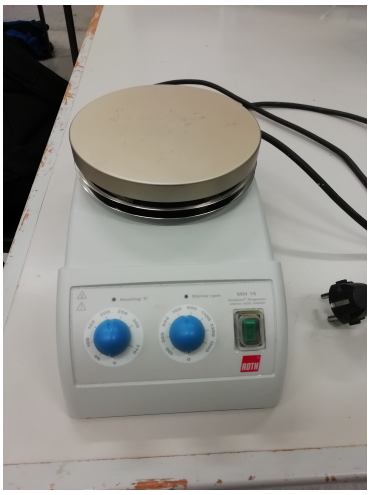

(b) *Rotilabo MH15* heating magnetic stirrer from *Carl Roth Gmbh*.

Figure 2.3: Equipments used in nanofluid sample preparation.

Characteristic	Value
Max. stirring capacity (H_2O)	15 L
Max. speed	1500 rpm
Motor rating input / output	30 / 23 W

Table 2.5: UP200Ht handheld ultrasonic homogenizer technical specifications

2.1.9 Syringe pumps

In order to perform the experiments, the continuous and dispersed phase fluids need to be injected into the device. For this, two syringes driven by syringe pumps were used, models *Nexus* 5000 and *Nexus* 6000 from *Chemyx Syring Pump Company*, as shown in figure 2.4. The inputs for the equipment were syringe diameter, working fluid volume and flow rate. With these parameters, the syringe pump software

imposes the adequate piston movement to meet the requirements. The technical specifications are displayed in table 2.6.

Table 2.6: *Nexus* 5000 and *Nexus* 6000 syringe pumps technical specifications.

Characteristic	*Nexus* 5000	*Nexus* 6000
Syringe volume	0.5μL - 140 mL	0.5μL - 225 mL
Maximum linear force	90.9 kgf	227 kgf
Precision	$\pm$1.0%	$\pm$0.35%
Reproducibility	$\pm$0.1%	$\pm$0.05%
Flow rate	1 nL/min - 200 mL/min	0.1 nL/min - 423 mL/min

Figure 2.4: *Nexus* 6000 from *Chemyx Syring Pump Company*

2.1.10 Microscope

The digital CMOS (Complementary metal–oxide–semiconductor) camera will be mounted on the microscope depicted in figure 2.5. It is the model CX41 with *UIS2* optical system from *Olympus* and it posesses 4 possible objectives (5x, 10x, 40x, 100x). Some important technical characteristics for the objectives availaible are listed in table 2.7.

Table 2.7: Technical characteristics of 1x, 10x, 40x and 100x objectives. WD is the vertical distance from the objective's front lens to the closest surface.

Objective PLCN	Numerical aperture (NA)	Working distance (WD)
4x	0.10	18.5 mm
10x	0.25	10.6 mm
40x	0.65	0.6 mm
100x	1.25	0.13 mm

2.1.11 CMOS camera

To acquire the images from the experimental tests, the CMOS *CR600x2* camera from *Optronis*, depicted in figure 2.6 is mounted on top of the microscope, and the software *TimeBench 2.3.1* records and manipulates the images. This software allows to control the exposure time, resolution, acquisition rate, number of images and other parameters. After recording, the images are exported to a laptop for subsequent analysis and post-processing. The technical characteristics of the camera are displayed in table 2.8.

Figure 2.5: Model CX41 with *UIS2* optical system microscope from *Olympus*.

Table 2.8: Image resolution as a function of the frame rate for the CMOS camera.

Image resolution (pixels x pixels)	Frame rate (fps)
1280 x 1024	500
1280 x 720	630
800 x 600	1250
512 x 512	2000
256 x 256	6000
128 x 128	15000

Figure 2.6: CMOS *CR600x2* camera from *Optronis*.

2.2 Experimental techniques and sample characterization

In this section, it will be provided a detailed overview of the sequencial steps performed during the fabrication of the devices and the methodologies required for the experimental tests. In this thesis, the overall microfabrication process includes the Aluminium (Al) coated glass hardmask by photolithography, the master by soft lithography and the microchannels by replica molding (Polydimethylsiloxane(PDMS) casting).

2.2.1 Microfabrication techniques in microfluidics

Although the first microfluidic devices were made by silicon and glass, much of the work currently performed by researchers takes advantage of soft lithography methods, specially based on master fabrication using photolithography and replica molding [49, 50]. In fact, the microeletronics and MEMS era was dominated by silicon fabrication techniques, particularly photolithography and etching methods, that started to be employed in microfluidic devices fabrication, but they revealed to be expensive and

time-consuming. Nevertheless, this revolution was important because their efforts resulted in a array of fabrication techniques that were further developed to include novel demands, like biological fluids [51]. Whitesides et al. [49] developed soft lithography methods in 1998, with the use of replica molding. This led to a quick transition to the main materials for microfabrication being elastomers, specially PDMS, and making it widely used in microfluidics. Besides being less costly, fast and easy to produce, PDMS devices also offer a number of good advantages for research, namely: good bio-compatibility; controllable surface chemistry; can seal irreversibly to itself or other materials; not toxic; high fidelity; optically transparent [50, 52]. Presently, a wide range of fabrication processes and materials for microfluidics exists, such as 3D printing and molding techniques, allowing researchers to take advantage of the most beneficial conditions for each application.

2.2.2 Materials

- **Mask**

  Photolithography serves as a complement of soft lithography by the need of an aluminium (Al) or chromium (Cr) coated mask. The mask is a transparent glass plate, with coated patterns of a material opaque to radiation - see figure 2.8 (b). The optically transparent regions contain the two-dimensional geometry of the microfluidic device [3]. The purpose of the mask is to filter the energetic radiation over which the photoresist will be exposed, that way transfering the patterns to the substrate.

- **Photoresist**

  In soft lithography, the master that determines the features of the microfluidic device is made of a photoresist emulsion layer. Due to its inherent properties, its considered a radiation sensitive material, whose properties change upon exposure to a certain energetic wavelength.

  For this work, it was used SU-8 50 epoxy-based photoresist from *Microchem*. As being a negative photoresist, it transfers a ”negative” of the pattern onto the wafer, meaning it will become less soluble to a certain solvent, due to cross-linking of their long polymeric chains (polymerization). Upon exposure, the parts that are in contact with the radiation will harden and the rest will get etched. The spin speed required as an input to the spin-coater in order to obtain an uniform height of 75 μm was taken from Figure 2.7, provided by the manufacturer.

- **Wafer**

  The wafer/substrate is a thin slice of a semiconductor material (usually Si) that will support the photoresist layer in common microfabrication techniques such as soft lithography. The wafer used in this work was a square Si sample with 0.7 mm thickness and 50x50 mm^2.

- **Developer**

  After the exposure process, the wafer is immersed in a suitable chemical (developer) that reacts with the not exposed SU-8 50, in order to remove it. For this resist, the developer used was PGMEA (1,2-Propanediol monomethyl ether acetate) by *Sigma-Aldrich*.

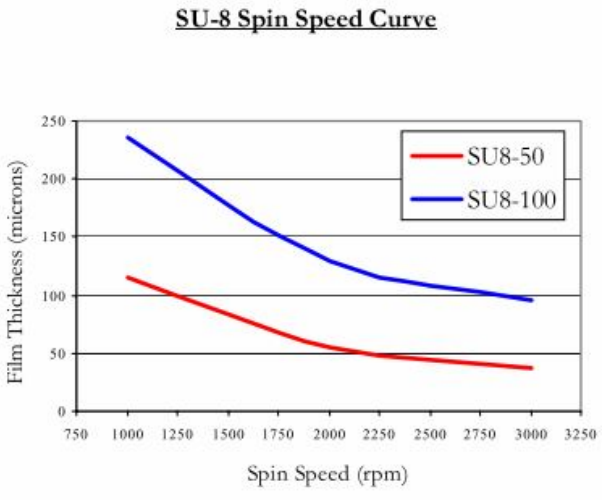

Figure 2.7: Film thickness of SU-8 photoresists as a function of the spin speed [53].

2.2.3 Fabrication of microfluidic channels

Glass hardmask for patterning

The 2D microchannels features were drawn in *AutoCAD* software and the features were printed in the thin Al film using Direct Write lithography by laser.

The process is initiated by preparing a glass sample of 50x50 mm^2, that is going to be used as a mask substrate. A sample with these dimensions needs to be accurately cut by the DAD321 Automatic Dicing Saw from *DISCO*. After, the substrate is cleaned using acetone, isopropyl alcohol (IPA) and rinsed with DIW. The sample is also dipped in a beaker filled with Alconox that goes into the ultrasonic bath for 30 min at 65° .

To perform mask patterning, the glass substrate needs to be coated with a thin 1000 Å film of aluminium. This is done by sputtering deposition (Physical Vapor Deposition (PVD) system) using *Nordiko 7000* from *Nordiko Technical Services Ltd.*, where the sample is placed inside a deposition chamber.

For the photolithography, the substrate is coated with 1.5 μm of a positive photoresist (PFR7790G27cP, from JSR Electronics) using the automated SVG Tracks system. This system performs a series of steps, from spinning the substrate with photoresist to ensure desired thickness and uniform coating, to a soft bake process after, at 85°C, to remove any solvents remaining.

The mask patterns are transfered using a Direct Writing Lithography machine (DWL), *Heidelberg Instruments DWL Lithography System*. This equipment performs exposure based on the mask layout on AutoCAD, by sweeping through the glass substrate and turning on the laser beam in the closed regions defined by the CAD file shown in figure 2.8 (a).

To complete the photolithography process, a developer (TMA238WA from JSR Micro) is used to remove the photoresist regions exposed to the laser. This step is again done using the SVG track system, with prior bake and cooling steps, to ensure the photoresist is hardened enough in the not exposed regions. Before advancing, the feature size and shape are verified under the optical microscope.

The final steps are wet etch the exposed aluminium, by dipping the substrate in a beaker filled with TechniEtch Al 80 MOS Aluminum etchant, and agitate it for a couple of minutes. The mask is finally

obtained by remove the left photoresist using acetone, as shown in figure 2.8 (b).

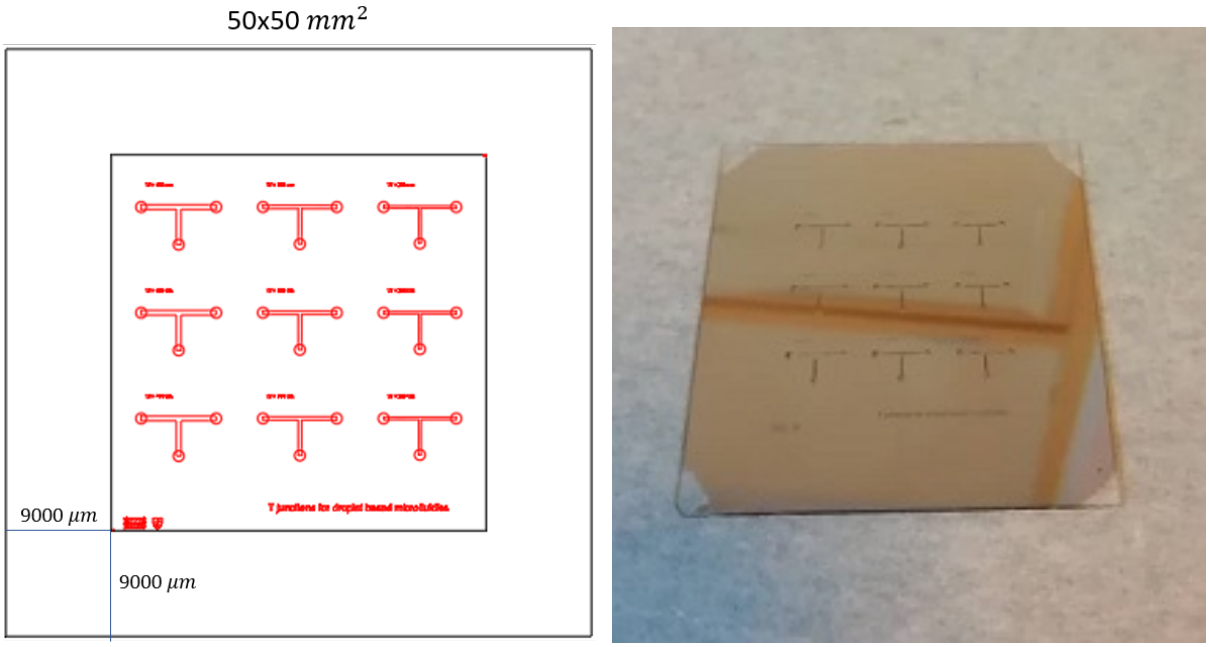

(a) CAD file with the T-junction geometrical features. Map must be exposed 9 mm away from the substrate since the sample size is 32x32 mm^2.

(b) Physical glass hardmask

Figure 2.8: Photomask (50x50 mm^2) with the T-junction geometrical features. The designed dimensions are displayed in table 2.13.

Soft lithography

Before applying the photoresist layer on top of the wafer, it should be cleaned and defect free. To this goal, the wafer is cleaned with acetone, IPA, DIW, with a similar procedure applied for the mask. A blow-off gun is also used to dry the substrate after cleaning. Before lithography is performed, the substrate is exposed to an oxidation treatment for 15 min in a UVO cleaner (5 min exhaust time), that removes contaminants by delivering sufficient UV radiation to dissociate/excite the respective molecules. This excited molecules are removed by reacting with atomic oxygen, also formed by dissociation of O_2 and O_3, and forming volatile molecules like H_20 and CO_2, which easily desorb from the surface.

Before the resist is applied, the cleaned wafer is subjected to a dehydration bake, to remove any excess water and increase the photoresist adhesion to the surface. The SU-8 negative resist needs to be uniformly spread on the surface since any thickness variations can cause problems during developing and subsequent resist removal. The rotational speed routines are defined according to the parameters delineated in 2.1.2, to get the desired 75 μm thickness. Resist application onto the wafer is done by pouring 1.97 mL (1 mL per inch of substrate diameter) on top of the spin-coater [53]. The spin-coating parameters are defined in table 2.9.

After these steps are finished, the system is subjected to a 2-step bake treatments. This guarantees the removal of solvent from the resist and densifies the film. Details can be consulted on table 2.10.

All parameters were determined by having as a reference the manufacturer's technical sheet and the calibration of the equipment used.

When the system is cooled to room temperature, its ready to go through the UV-light exposure for

Table 2.9: Spin-coater routines applied to the substrate with SU-8 resist to obtain uniform 75 μm thickness [53].

Step	Time (s)	Rotational speed (rpm)	Acceleration (rpm/s)
Spreading	10	500	100
Uniformization	30	1202	300

Table 2.10: Pre-bake and Soft-bake parameters applied [53].

Step	Temperature (°C)	Time (min)
Pre-bake	65	10
Soft-bake	95	30

125 s with a lamp energy of intensity 4.7 W/cm^2 and with the aluminium side in contact with the SU-8 photoresist facing upward, minimizing the gap between them. This allows the patterning of the 2D geometries onto the resist layer, by softening the photoresist in the regions of interest, as explained before.

The fabrication of the master ends with the post exposure bake and development stages. The parts of the photoresist not exposed are reacted with PGMEA applying strong agitation, until the resist is completely removed, and cleaning it afterwards with IPA. The post exposure baking routines are presented in table 2.11.

Table 2.11: Post exposure bake parameters applied.

Step	Temperature (°C)	Time (min)
Pre-bake	65	1
Soft-bake	95	10

PDMS Casting and PDMS membrane

In order to start the PDMS casting process, an appropriate mixture of PDMS and curing agent needs to be prepared, consisting of a 10:1 ratio, respectively, and vigorously mixed with a spatula. Since bubbles will form with the agitation, they need to be removed by placing the plastic cup containing the mixture in a vacuum-sealed desiccator for 1 hour or more, until no bubbles are present.

For the mold filling stage, 2 PMMA (Poly(methyl methacrylate)) plates, with 2 and 4 mm thick and 10 x 10 mm^2 area, were previously milled using a 2D CNC micromilling system, as shown in figure 2.9. These plates contain the inlet and outlet holes, and are to be taped and aligned with the SU-8 mold, defining the microfluidic chip structure and thickness.

After aligning the plates and tape the SU-8 mold, the pre-PDMS elastomer is poured carefully, to avoid formation and trapping of bubbles, with a syringe and LS20 tip. The injection is stopped when the mixture starts leaking and the connectors are inserted vertically into each hole all the way, as shown in figure 2.10 (a). The system goes through baking in an oven for 1h. The cured PDMS is then removed from the mold carefully with a scalpel and tweezers and cleaned with IPA and DIW, removing any PDMS residues and leading to the final product as depicted in figure 2.10 (b).

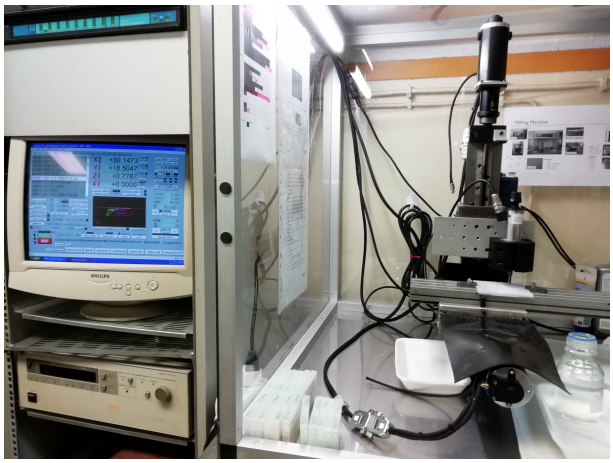

Figure 2.9: PMMA plate being machined using a 2D CNC micromilling system, according to the mold specifications.

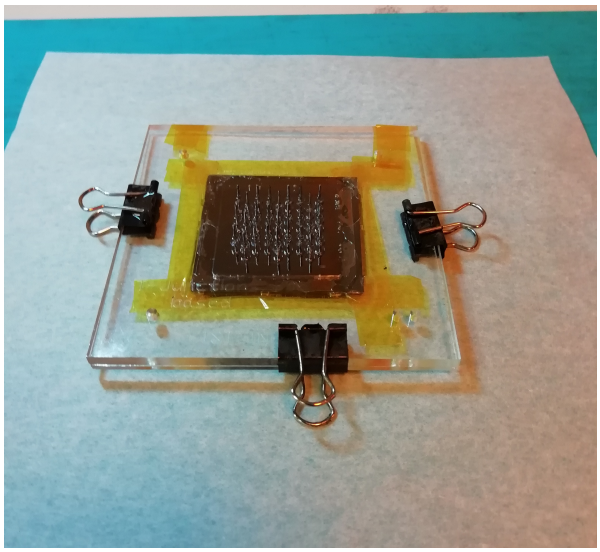

(a) Both PMMA plates and the SU-8 mold aligned and filled with pre-bake PDMS. Connectors are also fitted into the entry holes of the PMMA upper plate

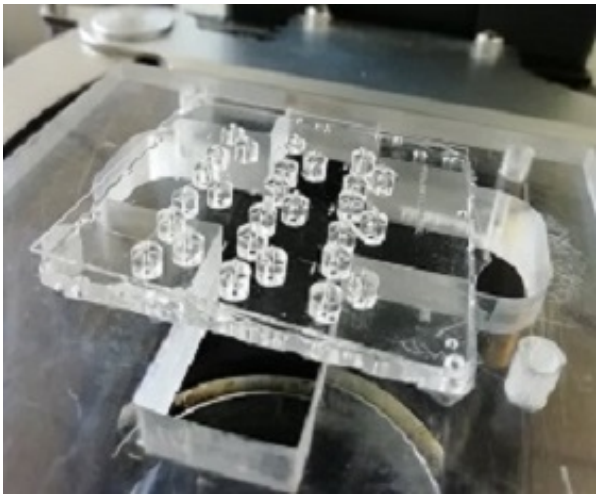

(b) Microfluidic device sealed and ready to be used.

Figure 2.10: PDMS casting process.

A simple schematics detailing the steps mentioned above is presented in figure 2.11.

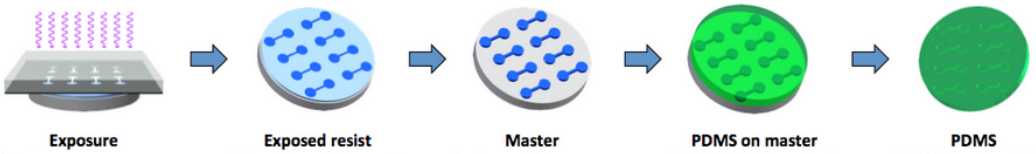

Figure 2.11: Steps performed to fabricate PDMS microfluidic channels by replica molding, starting from an SU-8 master. Source: UC Santa Cruz

The sealing of the microchannels is made with a PDMS membrane coating, ensuring uniform wetting properties in the microchannel, crucial for this work. This is done by spin-coating 1 mL (1 mL for each 1" substrate diameter) PDMS on top a Si wafer, after a dehydration bake, in order to obtain a 500 μ m uniform thickness. The spin-coater routines for the membrane are described in table 2.12.

Table 2.12: Spin-coater routines applied for the PDMS membrane coating.

Microchannel	Time (s)	Rotational speed (rpm)	Acceleration (rpm/s)
Spreading	5	250	100
Uniformization	20	250	100

The membrane is also placed in the oven for 1 hour at 70 °C to bake. The sealing of the microchannels is achieved by oxygen plasma treatment for 60s, using the *Harrick PDC-002CE* Plasma cleaner, with the contact surfaces for bonding facing up. This makes the surfaces hydrophilic by the creation of silanol ($SiOH$) groups in both surfaces. When the surfaces are brought into contact again, these groups will recombine to form a siloxane ($Si-O-Si$) covalent bond between both, that seals the structure. The channels are stored in a clean petri dish and allowed to bond for 24h, for permanent sealing, and are ready to use after this time.

2.2.4 Microchannels characteristics

In this thesis, 3 different T-junction geometries were fabricated as previously described. Their characteristics are presented in figure 2.13, where Γ is the aspect ratio of the main channel and Λ is the width ratio between the continuous and dispersed phase channels. Unfortunately, only two of them were tested, namely the T1 and T3, due to unexpected experimental problems on the T2.

Table 2.13: Designed dimensions for the T-shaped microchannels. h, Wc and Wd are the height, width of continuous phase channel and width of dispersed phase channel, respectively.

Microchannel	h (μm)	Wc (μm)	Wd (μm)	Γ	Λ
T1	75	200	200	0.375	1
T2	75	300	300	0.25	1
T3	75	400	400	0.1875	1

For research purposes, it is important to check the real dimensions of the geometries in order to characterize the quality and finishing. This can be done by performing a SEM (Scanning Electron Microscope) analysis and by the working optical microscope. For the latter, the calibration to calculate the real dimensions from the images captured by the CMOS camera was made with a 1 mm objective micrometer from *Nikon* and by using the free image processing software ImageJ. With the micrometer, it was possible to evaluate that, for the 4x microscope objective, the scale was 0.2581 pixels/μm.

From the images, it can be seen that the channels present good quality and, most importantly, a well defined perpendicularity at the T-junction walls, important geometrical feature for droplet formation. Moreover, it is important to notice that the wall's slope could also affect droplet formation. Even though this parameter is out of the scope for this work, it should be properly characterized using this type of analysis. It is also important to mention some discrepancy of the width values between the designed and real ones.

The height values were obtained using the profilometer described in section 2.1.3. The maximum

Table 2.14: Measured dimensions of the microchannels using SEM and optical microscopy analysis.

Microchannel	Method	Wc (μm)	Wd (μm)
T1	SEM	224	224
T1	Microscope	220	205
T2	SEM	334.5	327
T2	Microscope	330	310
T3	SEM	429	425
T3	Microscope	430	410

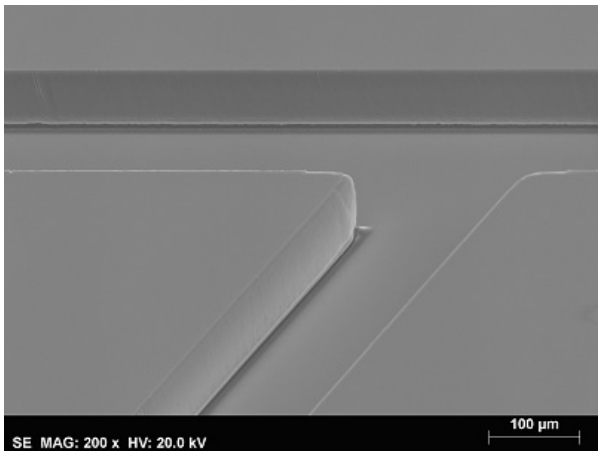

(a) Microchannel width = 200 μm (T1 geometry), 200x magnification

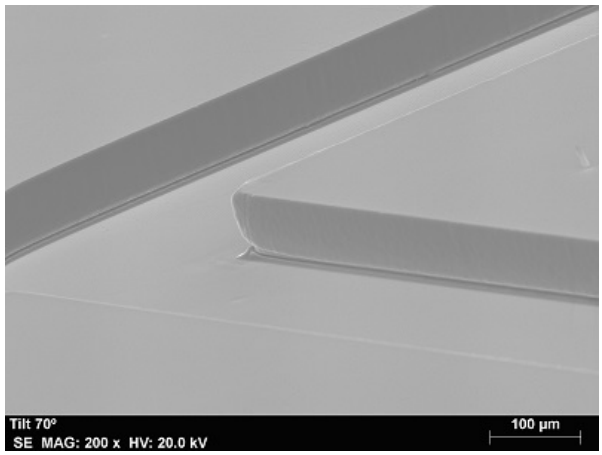

(b) Microchannel width = 300 μm (T2 geometry), 200x magnification

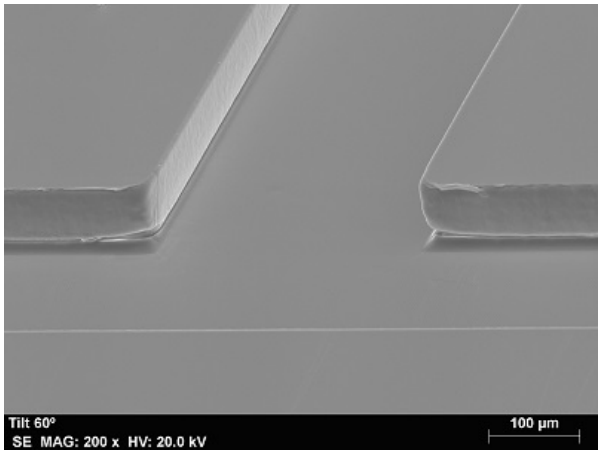

(c) Microchannel width = 300 μm (T2 geometry), 200x magnification

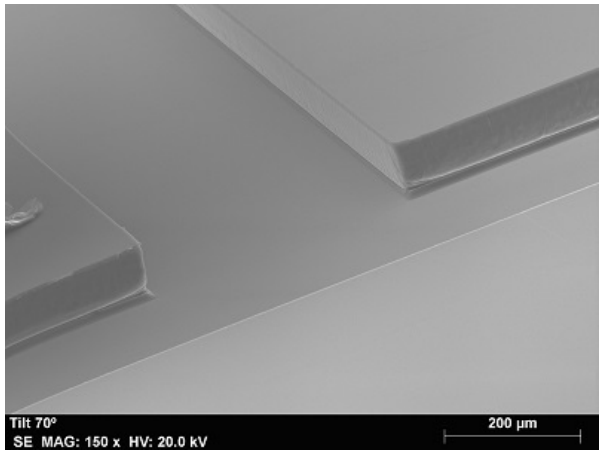

(d) Microchannel width = 400 μm (T3 geometry), 150x magnification

Figure 2.12: Images obtained with the SEM analysis.

difference between the designed values and the real values obtained was calculated to be 2.4%, reason why the value of h = 75 μm was used for the calculations.

2.2.5 Experimental tests methodologies

The setup arrangement for the experiments involves both the preparation of the working fluids and the necessary equipments. A schematics of the experimental setup is shown in figure 2.13.

The DIW and aqueous nanofluids were made fluorescent by adding 0.05 % w/w of fluorescein sodium

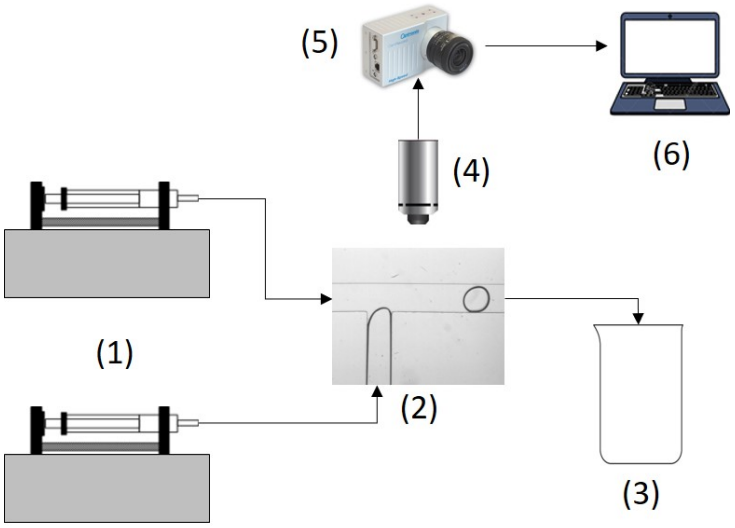

Figure 2.13: Experimental setup schematics. The dispersed and continuous phases are pumped by two separate syringe pumps (1) into the T-shaped microchannels (2), and the exit segment channel is connected to a deposit beaker (3). The microscope (4), which is connected to the CMOS camera (5), illuminates and captures the the amplified images, which are recorded by the camera and then exported for the working computer (6).

salt (*Sigma-Aldrich*). The connection from the syringes was made through polyethylene (PE) BTPE-90 tubing and 20-ga luer locks from *Instech*. Before pumping both fluids, the microchannels were first primed with the continuous phase liquid for 15 min. After this time, the pump was stopped and the dispersed phase one was turned on. When the dispersed phase fluid reached the T-junction, the continuous phase fluid was pumped again. An equilibration time was needed between flowrate variation, so the pressure in the channels was stabilized. The equilibrations spanned from 3-7 minutes, depending on the regime. In order to calculate the variables, like volume, several droplets (at least 10, depending on the formation time) were measured and then averaged, in order to get a better single value for a specific regime. This also allows the calculation of the polydispersity index. Formation times superior to the camera memory card space (around 7 seconds) were not measured. This was verified at low flowrate ratios and Ca numbers.

2.2.6 Working fluids characterization

The preparation of the working fluids demands a clear measure of their properties.

Nanofluid preparation

The preparation of nanofluids involved a two-step method. It was used aluminum oxide Al_2O_3 nanofluid from *Sigma Aldrich* with a nanoparticle content of 20 $\pm$ 1 mass %. According to the manufacturer, the size of nanoparticles is 30 nm, and this is assumed as true for this work. A proper dispersion was obtained by using the magnetic stirrer and the ultrasonic homogenizer, described in section 2.1. Before removing the nanofluid for dilution, it was placed in the magnetic stirrer for 20 minutes for homogenization. Then, the correct volume was measured in a beaker and dilluted with DIW, to get the correct nanoparticle content in volume %. The mixture was then subjected to ultrasonication, at 60 % amplitude

for 15 min in continuous mode operation. The sample was allowed to cool down at room temperature and then its properties were measured before using it in the experiments.

The experimental determination of the mass of nanoparticles m_{np} and the mass of base fluid m_{np}, was based on the following equation for mixtures:

$$\phi = \frac{\frac{m_{np}}{\rho_{np}}}{\frac{m_{np}}{\rho_{np}} + \frac{m_{bf}}{\rho_{bf}}} \times 100 \tag{2.1}$$

where ϕ is the nanoparticle volume percentage (%), m_{np}, ρ_{np}, m_{bf} and ρ_{bf} are the mass and density of nanoparticle and base fluid, respectively. This allows for the calculation of the mass of powder, to get the desired volume % of nanoparticles in the nanofluid, $\frac{m_{np}}{m_{bf}} = \frac{\phi}{1-\phi} \times \rho_{np} V_{bf}$, where V_{bf} is the volume of base fluid.

Dynamic viscosity

The dynamic viscosity was measured using the *LVDV-II+Pro* set from *Brookfields Engineering* viscometer, as described in section 2.1.5. The viscometer is connected to a computer and the software Rheocalc 32 was used for external mode computer control. The viscometer was calibrated by measuring the DIW viscosity at room temperature, and comparing with according literature. The measured dynamic viscosities are presented in figure 2.14 for all working fluids.

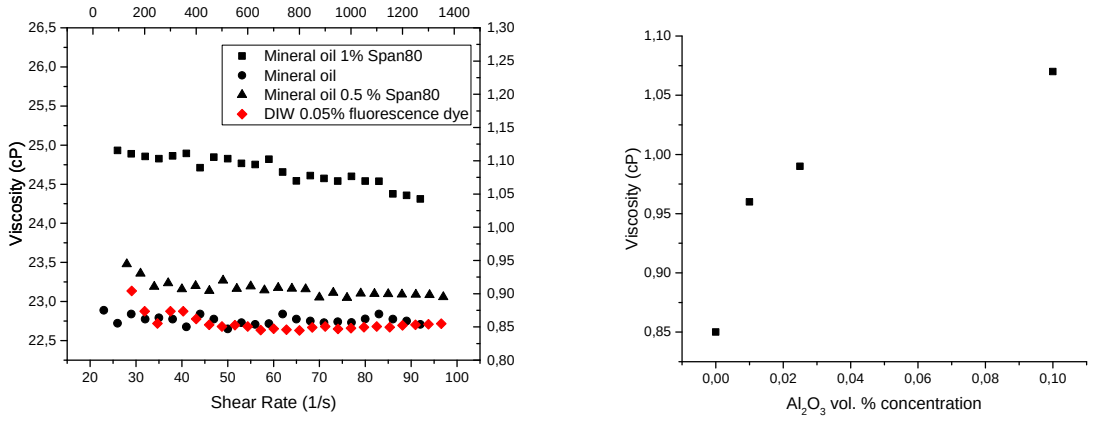

(a) Measured dynamic viscosity for DIW w/ 0.05% w/w fluorescent dye (Top X/Right Y) and mineral oil with different concentration of Span 80 (Bottom X/Left Y).

(b) Measured dynamic viscosity as a function of the vol. % concentration of Al_2O_3.

Figure 2.14: Dynamic viscosity values obtained for the working fluids.

The dynamic viscosity of DIW was found to be 0.85 cP, while the viscosity of mineral oil is 22.7 cP. As expected, the values for the mineral oil with the addition of Span 80 surfactant were found to increase since this compound has higher viscosity. The working fluid for the continuous phase is the mineral oil with 1 % Span 80, with an averaged measured viscosity of 24.7 cP, value used for the calculations. These values are in accordance with literature data [43, 54]. On the other hand, the viscosity of DIW was also verified to increase with the addition of nanoparticles, a trend verified by other authors [55]. The values of viscosity will be presented in tabular form in chapter 4.

Interfacial tension

The interfacial tension was measured using the *Attension Theta* optical tensiometer, as it was described in subsection 2.1.6. Besides calculating the interfacial tension, it was also important to verify the wetting properties of the PDMS material of the microchannels. The sealing of the microchannels using oxygen plasma treatment, as it was explained in subsection 2.2.1, renders a surface to become hydrophilic. In order to achieve water in oil droplet formation, the surface must be hydrophobic. However, this treatment is temporary, naturally reverting itself in several hours, after bonding is achieved. It is also typical to apply a heat treatment in an oven to accelerate the process [56–58]. For this purpose, the sessile drop method was used to calculate the static contact angle of both the distilled water and mineral oil. A slab of the prepared PDMS used on the microchannels was placed on top of the table, and the dispenser needle correctly adjusted to the camera - see figure 2.15 (b). Three separate measurements for 3 different drop volume sizes between 1 to 10 μL were performed, and the average static contact angle was determined. As it can be seen in figure 2.15 (a), the programme measures 246 contact angles (123 each side), by recording at 12 fps over the course of 10 seconds the droplet behaviour on top of the surface. The results for the static contact angle of DIW and mineral oil, after averaging for three different volume drops, were 110.35° and 44.60° , respectively.

The wetting behaviour of the PDMS was verified sucessfully, and the surface is hydrophobic and oleophylic as expected.

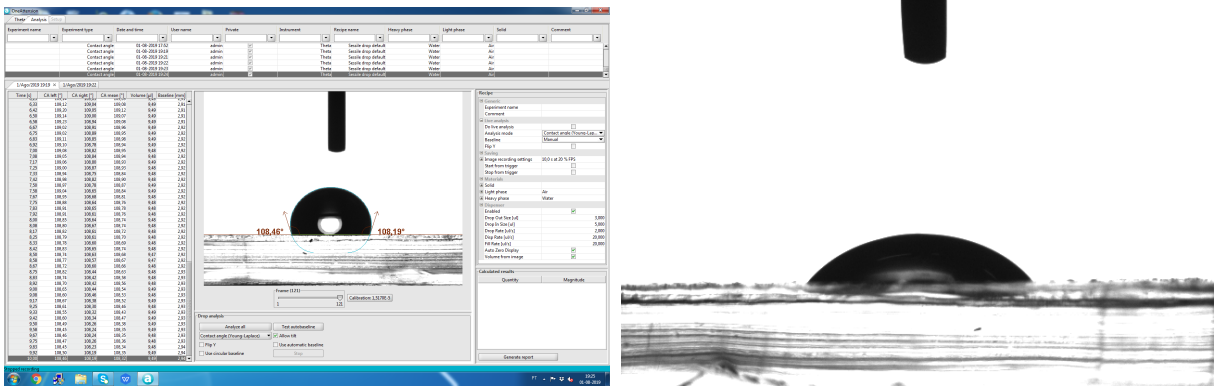

(a) Sessile drop method for the calculation of the static contact angle of DIW on PDMS.

(b) Static drop of mineral oil on top of a PDMS surface.

Figure 2.15: Sessile drop method for the calculation of the static CA of DIW and mineral oil on a PDMS surface, using the optical tensiometer and the software *OneAttension*.

The interfacial tension between both liquid phases was calculated using the pendant drop method. To ensure the measurements were accurate, some calibration tests were performed at room temperature, and compared with known experimental data from literature, namely the surface tension of DIW and mineral oil and the interfacial tension between DIW and mineral oil. Before each test, the syringe and needle were both washed with DIW three times to prevent nanoparticles from clogging the tubes.

Using the pendant drop system - see figure 2.16 (a) - to calculate the interfacial tension between two liquids requires the needle to be immersed in the less dense liquid (light phase) in order to a drop to be

stably formed. On the other hand, a specific container needs to be used since the software needs to capture well the shape of the drop in order to run the algorithm. With this in mind, the mineral oil used in the experiments was poured in a *Starna* glass spectrophotometery cell , and a DIW drop was generated inside, as depicted in figure 2.16 (b). This method proved reliable by comparing the obtained measured values with the existent data [59–61], as the surface tension obtained for DIW and mineral oil are 71.40 mN/m and 29.70 mN/m, respectively, and the interfacial tension between DIW and mineral oil is 49.88 mN/m.

(a) DIW surface tension measurement using pendant drop method.

(b) DIW drop formed inside the optical glass cell filled with mineral oil.

Figure 2.16: Pendant drop method for the calculation of the liquid-liquid interfacial tension using the optical tensiometer and the software *OneAttension*.

The data obtained for the interfacial tension measurements of the nanofluid dispersions is plotted in figure 2.17.

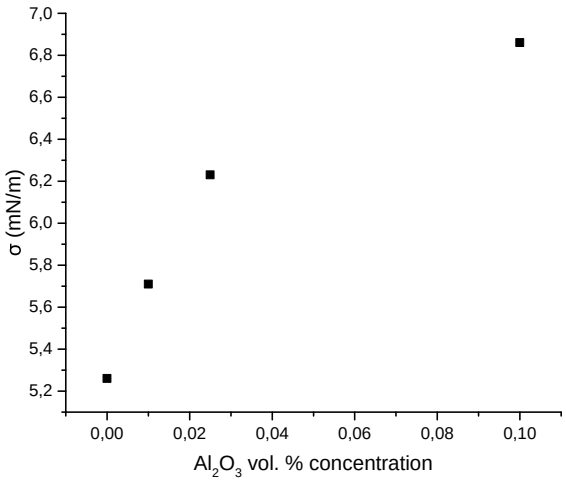

Figure 2.17: Interfacial tension measurements for the Al_2O_3 dilute nanofluid for different concentrations in volume %.

Interestingly, an increase of σ is observed for all the concentrations tested. Although this is not a usual trend since most of nanofluid studies show the opposite behaviour, similar results for surface

tension of Al_2O_3 diluted nanofluids were previously published [62, 63]. The values of interfacial tension will be presented in tabular form in chapter 4.

2.2.7 Syringe pump calibration

For this type of experimental work, the flowrate is a crucial independent variable. It is important to perform a syringe pump calibration in order to minimize equipment related experimental deviations. Particularly, for the case of the plastic syringe pumps, the flow rate dependent pressures associated, may cause the syringe to deform elastically, as it is not rigid enough to withstand such stresses [54]. For this reason, glass syringes were used, namely the 5 mL syringes from *Hamilton*. The calibration was made for the full range of flow rates used for the experiments, between 60 µl/min and 0.025 µl/min and it was done by comparing the volume poured into a graduated beaker by the equipment with the theoretical volume that is a function of the input flow rate value selected in the pump software.

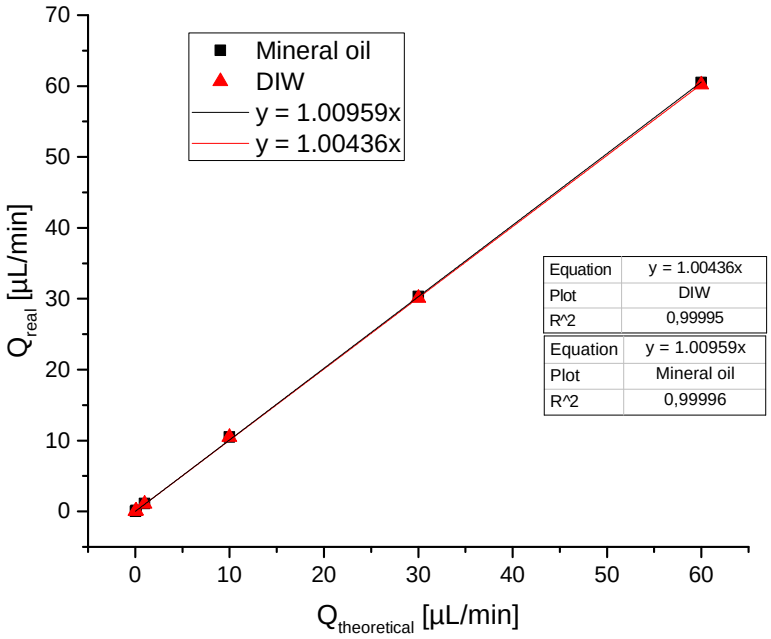

Figure 2.18: Relation between the real flowrate pumped using the syringe pumps N5000 (Mineral oil) and N6000 (DIW) and the theoretical flowrate expected from the input.

Associated errors with the calibration are related with the reading of the volume values of the beaker. Two different beakers were used: a 1 mL beaker for the lowest flowrates and a 10 mL for the larger ones. The associated errors with this type of measure are half of the smallest division scale of each beaker, which are 0.0125 mL and 0.1 mL, for the 1 mL and 10 mL beakers, respectively.

The real flowrate is then calculated using the equation 2.2:

$$Q_{exp} \pm e_{abs} = \frac{V_{real}}{\Delta t} \pm \frac{\text{Half of the smallest division scale}}{\Delta t} \tag{2.2}$$

From the figure 2.18, a very good agreement of the values for DIW and mineral oil is attained, so no further corrections were employed and the values given as input were the ones used for the calculations.

Chapter 3

Digital image processing

As it was mentioned in chapter 2, the droplet imaging is made using the CMOS camera that is connected to the microscope. This set captures sequential images of the droplet formation process and allows, after some analysis and post-processing, the retrieval of important information regarding the occurring physical phenomena and parameters relevant to this study. However, it is crucial to develop an algorithm to perform a digital treatment of the images. Furthermore, the calculation of important parameters based on these images, also requires to be coded.

To achieve these goals, a *MATLAB* (Mathworks) code was created with two functions: remove unwanted noise from the image and calculate the parameters based on the 2D droplet shape.

3.1 Basic principles

Digitally, a 2D image is a finite function representation $f(x, y)$ where x and y are finite spatial coordinates and where f represents the brightness at a certain point. The conversion of the image into a rectangular integer matrix allows for its representation, processing and manipulation using a software, like *MATLAB*. Each element of this matrix is called picture element or pixel, and the value that it contains is the pixel intensity.

In *MATLAB* environment, there are 4 different types of digital images, where only 2 are of interest for this work: grayscale images and binary images. The images captured by the camera are monochromatic, meaning they will be captured using a grayscale. The cell values for the matrix of a grayscale image can only take a limited range of intensities, for each pixel, that depends of the memory class used. For this case, such scale goes from 0 (black) to 255 (white), since the image obtained is from the class *uint8*, and the values in between are different gray intensities. For binary images, each pixel is stored as 1 bit with only 2 values, 0 and 1, which for this case, represent black and white, respectively.

3.2 Image treatment

Contrast/intensity adjustment

In order to improve image definition and contrast, it is useful to perform a proper redistribution of the pixel intensities to more extreme values, in order to cover a wider range of these, increasing the contrast of the original image. This is important since the images obtained from the experiments only covered a relatively small range of intensity values, which makes their analysis a more complex task. To this end, the function *imadjust* from *MATLAB* Toolbox is used. By default, *imadjust* saturates the bottom 1% and the top 1% of all pixel values, as shown in figure 3.1. Both images, before and after the contrast adjustment, are displayed on the left side (figure 3.1 (a,c), with their respective pixel histograms (figure 3.1 (b,d)). The remapping of intensity values to the full range is clearly observed from the latter, allowing for a better image constrast, and providing a better shape highlight of the fluids interfaces, marking the droplets in the process.

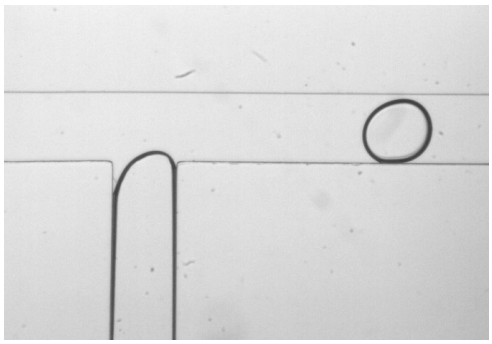

(a) Original image.

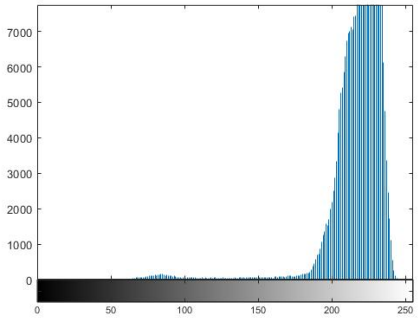

(b) Pixel histogram of the original image.

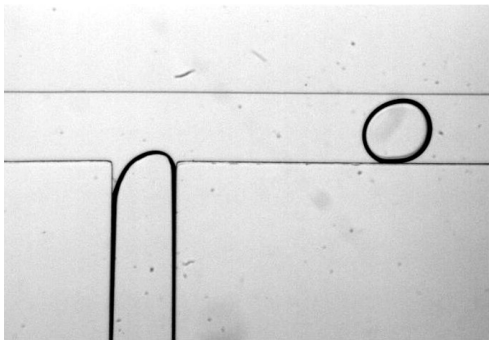

(c) Adjusted image.

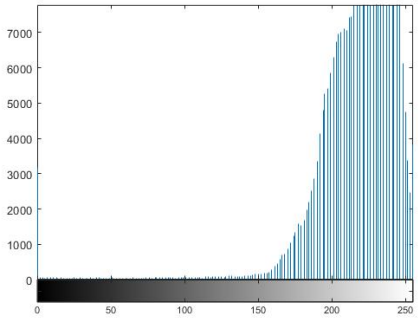

(d) Pixel histogram of the adjusted image.

Figure 3.1: Intensity adjustment of the images by using $imadjust$ function, and their respective pixel histograms. Width of the channel equal to 200 μm for scale.

Microchannel wall detection and noise removal

Different brightness matrices are obtained for every experiment and intensity values outside of the walls can also be transformed into a 0 bit value when performing the binarization. Such values represent "noise", and can be deleted by using the functions *bwareopen* and *imclose* from the Toolbox. The function *bwareopen* removes all connected components that have fewer than a certain amount of pixels, defined by the user, that way removing small isolated objects. On the other hand, the function *imclose*

connects determined objects by a morphological operation of dilation followed by erosion, using a certain structuring element created by the user. This function was applied to the external regions of the channel, assuring an uniform clean section. This method can then be applicable to all images, only changing the threshold parameters. To finalize, the application of an adaptive low-pass Wiener filter *wiener2*, further improves image quality, by executing intensity smoothing according to local image variance. For small local variances, the smoothing performed is large and, for large ones, the smoothing is small, that way preserving droplet edges and walls while removing noise. The final results of the entire operation is shown in figure 3.2.

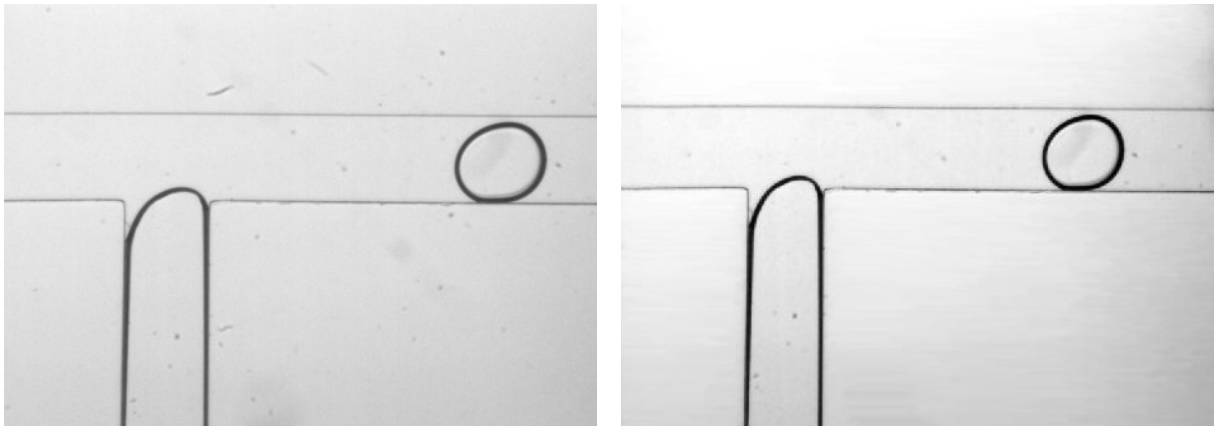

(a) Original image (b) Final image obtained with the image treatment code

Figure 3.2: Illustration of the final image obtained with pixel treatment done to the images from the experimental tests. Width of the channel equal to 200 μm for scale.

3.3 Droplet detection, filtering and measurement

In order to obtain the droplet volume, it is necessary to analyze the 2D droplet shape images captured during the experiments. A lot of different methods can be used to estimate these variables; however, the attainment of an accurate value is difficult, since it is mandatory to perform specific simplifications regarding the curvature of the droplet in the height direction plane, since this shape is totally unknown [23].

General overview

For this thesis, the channel geometries fabricated have aspect ratio $\Gamma < 0.335$, so, in the squeezing regime, where L $>$ h, a reasonable assumption is that the slug almost fully occupies the section, in the height direction, and smooth side curvature is obtained due to interfacial tension, so it will look like a disk. In the dripping regime, typically either L $\sim$ h is observed or L $<$ h, and a perfectly spherical shape can be assumed. For the latter, the droplet length L is the diameter d, and the volume calculation is trivial. As it will be seen in chapter 4, the perfect curvature of the slugs is not always observed.

Nevertheless, it is important to point out the problematic situations that can affect data collected with the experiments. Although it appears to be common sense that the height of the droplet is equal to the height of the channel for the squeezing regime, this is definitely not true since a thin film of continuous

phase must exist in between due to non-wetting properties of the dispersed phase. Also, since the channels were made with PDMS, swelling can occur since a mineral oil is used and flexing of the PDMS due to pressure-driven flow pumping method has been observed by other authors [23, 64]. However, the dimensions of the channels are bigger compared to typical microfluidic devices, so these problems are expected to have less effect on the data obtained.

Droplet measurements

As it was said previously, a MATLAB programme was created to get this data. As with most edge detection routines, this code works by isolating the droplets in a binary image and calculating the 2D area, in pixels, and converting it into volume and length by appropriate dimension transformations. The original image is subjected to a binarization by thresholding or intensity-gradient methods, allowing the detection of the droplets boundaries. An histogram of the original image is also plotted, to help in the choice of the threshold value. An initial option to crop is presented as well since the binarization of the full image sometimes is not totally trivial, and a single droplet can be measured more easily. More than one droplet can be present in the image, so a labeling command is used to identify each one. The calculations are carried out by pixelization commands, that determine the centroids, area and length. All these processes are followed in the main window, as shown in figure 3.3.

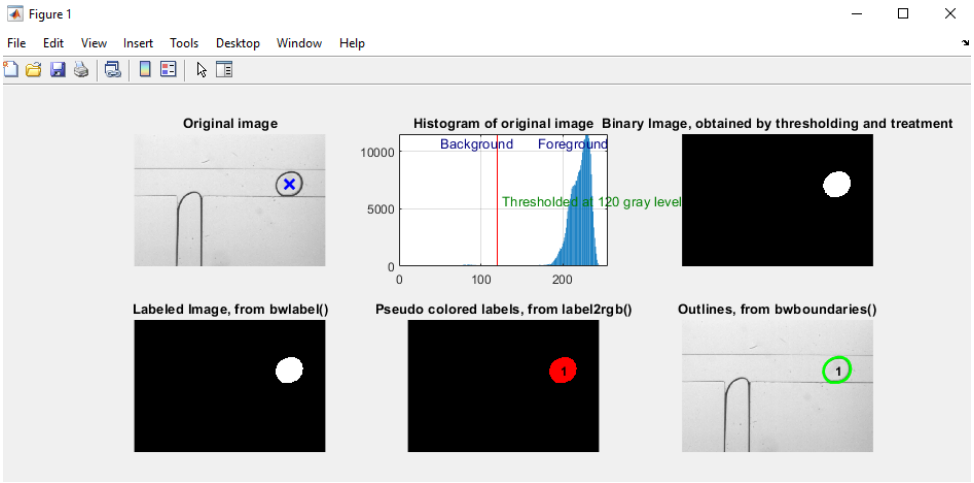

Figure 3.3: Main figure obtained with the MATLAB code. The image threshold binarization, filling, labeling and contouring is shown.

As it can be seen in the histogram, the value at the right represent the brighter pixels, that are of no interest and will be transformed into black intensity. The threshold value will be chosen inbetween the dark and bright intensity values of the original image, only capturing the walls and fluid interfaces. Since punctual low intensity value noise may appear in the images, a *bwareaopen* commad is previously applied, in the same way it was used in section 3.2. Next, the walls and the dispersed phase thread are deleted using the *imclearborder* command, that clears brighter objects connected to the border. The final image detects only the droplet pixels, allowing measurement of their properties using the *regionprops* function.

This method is not always straightforward and presents some challenges. The precision of this type of algorithms depends on many factors such as video resolution, frame rate, working distance and phase

contrast [65, 66]. The boundary contrast can be improved by using fluorescence, proper illumination and working distances close to half the height. Other important parameter regards the camera itself, such as the camera exposure time and frame rate also influence image quality. Large exposure times have the disadvantage of blurring fast moving blobs, such as in figure 3.4.

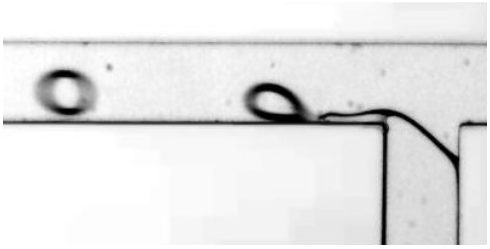

Figure 3.4: High speed droplet formation. Width of the channel equal to 200 μm for scale.

In MATLAB environment, this problem is avoided by using two separate thresholds, to detect connected weak and strong edges, known as the *Canny* method. This proved to be effective and it was used in such cases.

To better visualize each droplet, an option to extract individual droplet images is given. Each droplet is plotted, individually, and the Equivalent Circular Diameter (ECD), area and volume are displayed, in pixels, as shown in figure 3.5. The droplet ECD is calculated by getting the diameter of a perfect circle with equal area.

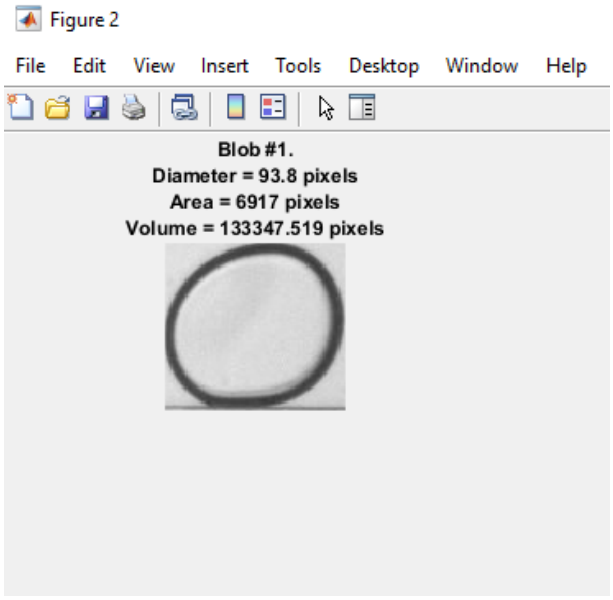

Figure 3.5: Individual droplet images extracted, containing the values of the Equivalent Circular Diameter, Area and Volume, in pixels.

According to the previous discussion, the droplet volume is calculated in 2 different ways, depending on the droplet length: if L $<$ d, then a spherical droplet is assumed and the equation for the volume of a sphere with L = d is used, while if L $>$ d, the 3D volume is reconstructed from the 2D image from the following expression [26]:

$$V = hA - \frac{h^2 P}{2}\left(1 - \frac{\pi}{4}\right) \tag{3.1}$$

where A and P are the 2D area and perimeter of a single droplet, respectively, and h is the channel height. This equations accounts for the total volume occupied by the length of the droplet and subtracts the volume associated with the side curvatures, by assuming these last equal to $\frac{h}{2}$ - see figure 3.6 - and that the droplet is perfectly symmetrical to the center of the microchannel.

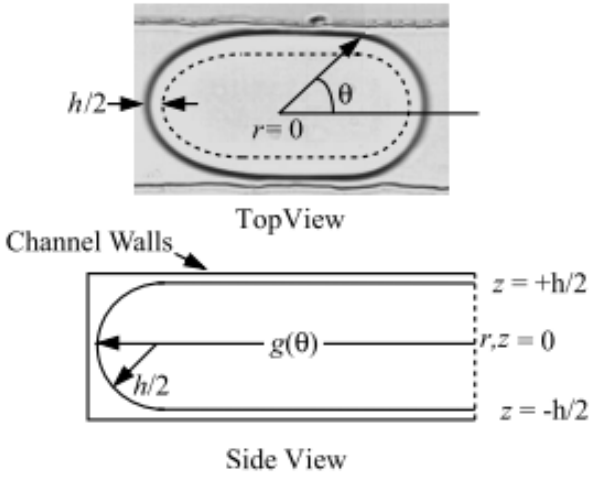

Figure 3.6: Sketch of the 3D droplet model assumed from the 2D projection in the images, where the side curvature is assumed to be equal to $h/2$. Adapted from [23].

As with all simplified equations, it has errors associated with it, specially because the perfect $\frac{h}{2}$ curvature is not always verified. This is expected to be a problem for low interfacial tension fluid pairs, such as it is the case for this work. For this reason, the dispersed phase fluid flowrate Q_d will be calculated using data from this equation, as it will be explained below.

Finally, the code also computes the droplet length and the maximum distance from the boundary contours, as shown in figure 3.7. Both are visualized in a figure window to ensure the code is properly capturing them.

Dispersed flow rate calculation

The continuous and dispersed phases are both pumped into the microfluidic device by using syringe pumps, with the desired the flowrate being the independent parameter. The accuracy of the algorithm was tested by calculating Q_d based on droplet formation time and volume, the latter given by equation 3.1. Since the pixel to micrometer constant is already known, the volume in pixels is transformed into SI units. This value is then compared with the theoretical value given to the pump, to test the accuracy of the code. Results will be presented in the next chapter.

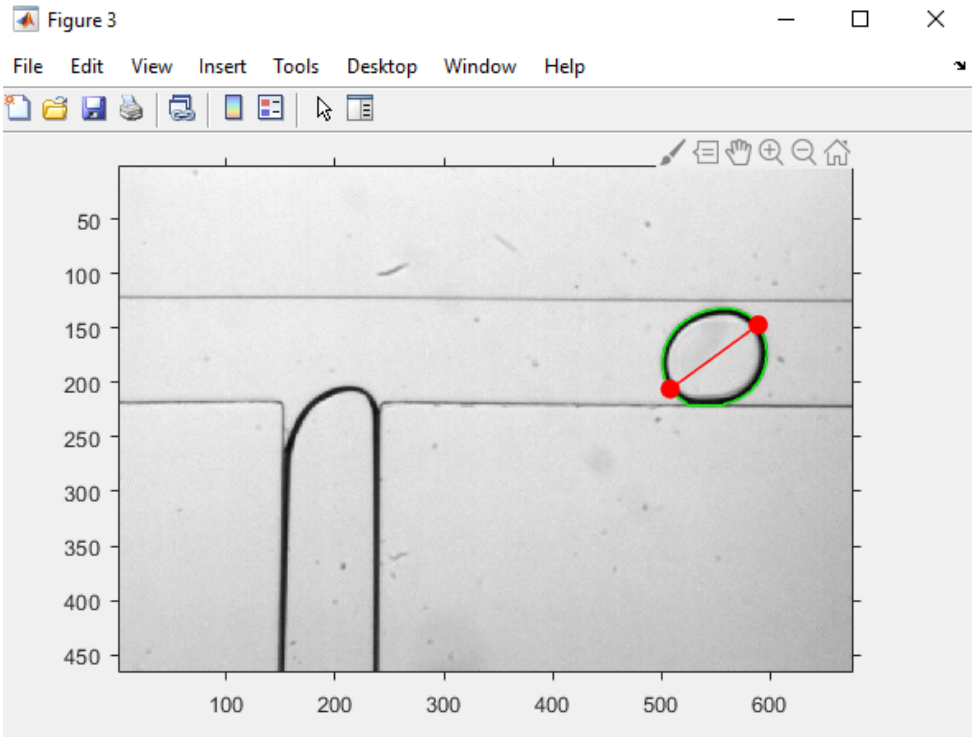

Figure 3.7: Droplet length (in the flow direction) and maximum distance (drawn in red) measurements from droplet contour. Width of the channel equal to 200 μm for scale.

Chapter 4

Presentation and Discussion of the Results

As stated in chapter 1, the aim of this thesis is to characterize droplet formation parameters in a T-junction, with DIW and Al_2O_3 aqueous nanofluid as the dispersed phase and mineral oil as continuous phase. The working fluids used in the present work are physically described in table 4.1. For each T-channel, the experiments performed with different flowrate ratio Q, Capillary number of the continuous phase Ca_c and Γ are those presented in table 4.2. The Capillary number Ca shown in the table, as before, without subscript, refers to the Ca of the continuous phase fluid Ca_c, which properties (viscosity μ and interfacial tension σ are fixed for each dispersed phase fluid) and its variation only depends on the flowrate Q_c imposed.

The densities for the nanofluids were not calculated since, as it was mentioned in the bibliographic review, the density ratio is almost equal to 1 for liquid-liquid droplet formation. Furthermore, their values are expected to increase negligibly with the concentrations of the nanoparticles since the ones used are very small.

Table 4.1: Physical properties of continuous and dispersed phase fluids used for this work. The Capillary number Ca shown in the table, as before, without subscript, refers to the Ca of the continuous phase fluid Ca_c.

Fluids	Viscosity μ (mPa.s)	IF σ (mN/m)	Density ρ (Kg/m^3)
Mineral oil 1% Span 80	24.7	–	860
DIW 0.05 % fluorescent dye	0.85	5.26	973.44
DIW 0.01 vol. % Al_2O_3	0.96	5.71	-
DIW 0.025 vol. % Al_2O_3	0.99	6.23	-
DIW 0.1 vol. % Al_2O_3	1.07	6.86	-

With this range of experimental variables, it was possible to assess the impact of Q and Ca on droplet formation and in separate droplet formation modes. This range of Ca encompasses three distinct droplet formation regimes, specifically the squeezing, transitional and dripping regimes, in which their identification, relevant phenomena and physical description are of great importance to fully understand

Table 4.2: Parameters to be varied in the experimental tests.

Exp. parameter	Range values
Q	0.01 - 0.8
Ca	0.002 - 0.1
Γ	0.176 and 0.335

droplet generation process for DIW and Al_2O_3 aqueous nanofluid.

For all experiments, the flowrate ratio Q was changed by keeping the continuous phase flowrate Q_c constant, while varying the dispersed phase flowrate Q_d. Moreover, by doing this for several values of Q_c, it allows to assess the influence of Ca on droplet size and formation time for different flowrate ratios. The geometrical influence of Γ was verified by testing in two separate fabricated geometries, specifically T1 and T3 (see table 2.14). In order to better understand the mechanisms of droplet formation, the details of the droplet growth evolution will be displayed for each regime and for specific Ca and Q conditions.

It is important to notice some of the flowrate ratios Q were not tested for a particular Ca, since they corresponded to either an impossibility imposed by the lowest flowrate that the syringe pump can provide, for lower Ca numbers, or an irregular droplet formation, for higher Ca numbers.

4.1 Distilled water droplet formation

4.1.1 Influence of the flowrate ratio

As it was described, the influence of the flowrate ratio Q on droplet formation was investigated for several Ca numbers displayed in table 4.2 and for two geometries. Experimentally, this meant changing the dispersed phase flowrate Q_d, while keeping the continuous phase Q_c constant, according to the parameters and fluid properties measured.

In figure 4.1, the full results obtained for the non-dimensional droplet volume V' are plotted, for each Ca and for each geometry, against the values of the flowrate ratio Q.

The results of both plots of figure 4.1 clearly evidence that the non-dimensional droplet volume V' increases, for all the Ca and geometries tested, with the flowrate ratio Q. It is possible to detect the existence of a change in regime from this type of graph, since one can clearly notice a decreasing variation of V' on Q, as the Ca of the continuous phase reaches higher values.

This behaviour, due to the conditions at which it occurs, has also been reported in literature and, therefore, is expected, since at smaller Ca numbers, droplet formation is in the squeezing regime. In both geometries, a purely squeezing regime was observed for Ca = 0.002 and Ca = 0.005. Snapshots of the squeezing regime at the T1 geometry are depicted in figure 4.2.

Broadly, the forming DIW interface is observed to grow freely because the mineral oil flowrate is very small and the tangential shear forces exerted are not sufficient to deform it before it fills the entire channel. As it grows, the interface restricts the continuous phase fluid path through the small gaps around it, reducing the available flow area and increasing locally it's velocity and dynamic pressure. The

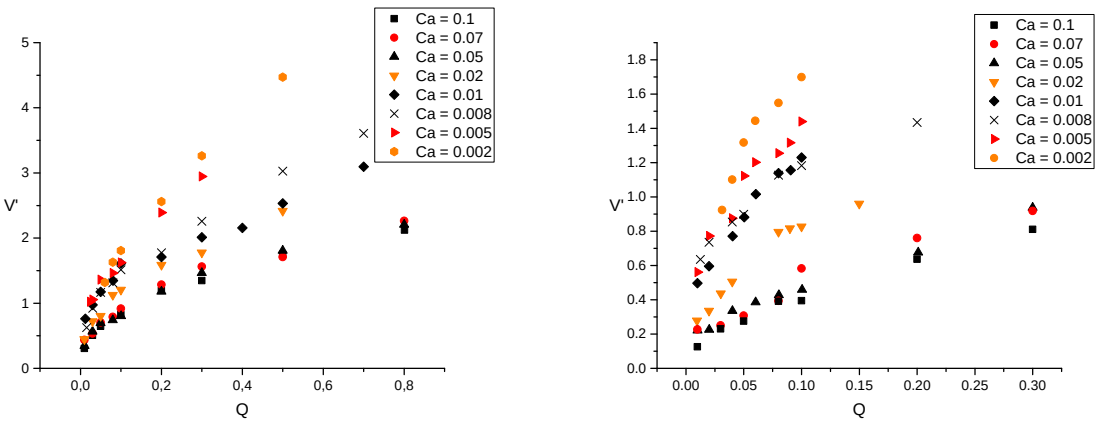

(a) $\Gamma = 0.335$ (b) $\Gamma = 0.176$

Figure 4.1: Variation of the dimensionless droplet volume V'= V/W_c^2h as a function of the flowrate ratio $Q=Q_d/Q_c$, for different Ca and for both geometries.

consequence of this event is an increase of the static pressure upstream of the advancing DIW stream, due to a deflection of the continuous fluid flow. The pressure difference established downstream and upstream of the attached thread, creates a strong necking force at the interface, which is the inducing break-up factor in this regime. Gradual necking is verified until it detaches at the T-junction. After detachment, the thread is noted to recede a small distance into the dispersed phase channel before starting its advancing towards the T-junction to repeat the cycle. This is visible in the last 2 pictures from figure 4.2, and it is indicated with a red arrow. This lag mechanism was also studied by Glawdel et al. [27] for the transitional regime, therefore including an additional step into the formation process of a droplet, consisting of lag, growth and necking stages and is here further extended to the squeezing regime, for small flowrate ratio Q and aspect ratio Γ conditions. For this squeezing regime, it was also observed that the interface always ruptured at the T-junction, for all Q and Ca conditions.

Considering the 2-stage linear scaling law proposed by Garstecki et al. [22] (see equation 1.10) for the squeezing regime, the data for Ca = 0.002 and Ca = 0.005 seems to find reasonable agreement to the function V' = 0.95 + 7.2Q (R^2=0.9919), as depicted in figure 4.3.

On the other hand, data obtained for the T3 geometry does not correlate well with this fitting. Interestingly, a linear behaviour is observed for $Q < 0.06$, but with a decrease in the constant of proportionality of 33 % for Ca = 0.005. This shows that changing the aspect ratio also leads to a distinct pressure difference behaviour obtained between upstream and downstream sides of the protruding thread.

For increasing Ca of the continuous phase, droplet formation entered the dripping regime, observed at $Ca > 0.02$ for both geometries. In this regime, the effect of the upstream pressure forces start to become less significant and shear stress exerted on the interface gains the role of the dominant detachment mechanism, with the increase of Q_c. Again, in figures 4.4 to 4.7, droplet formation evolution is shown for different time instants and for Ca = 0.1 and Ca = 0.05.

Contrary to the squeezing regime, the dispersed phase thread does not fill the entire main channel due to the higher shear forces exerted during the growth stage, which causes it to deform apreciably as

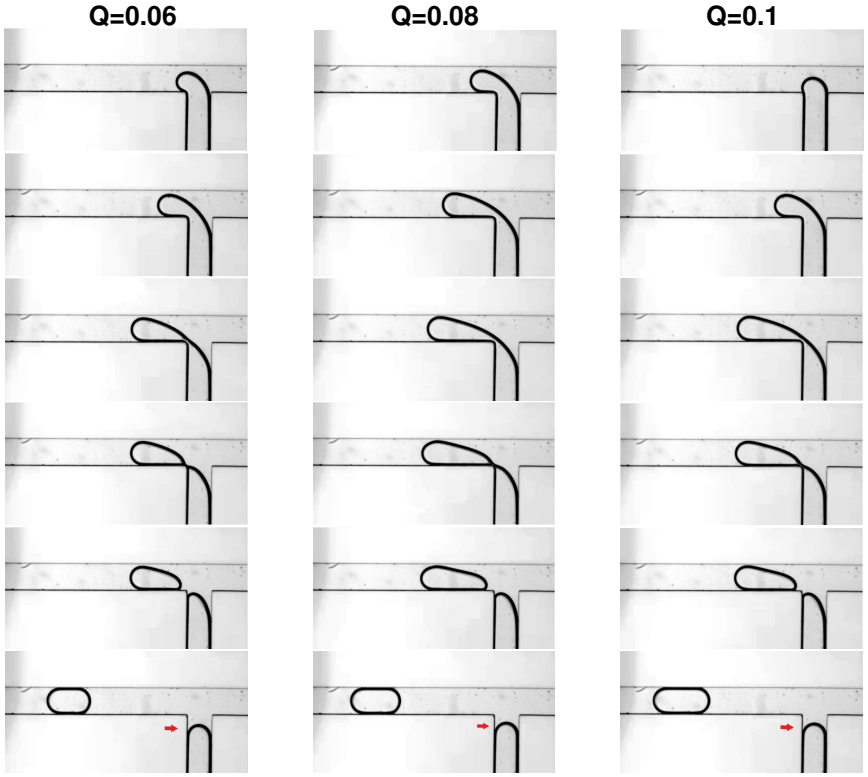

Figure 4.2: Droplet formation process in the squeezing regime for Q = 0.06, 0.08 and 0.1, at Ca = 0.002, for the T1 geometry.

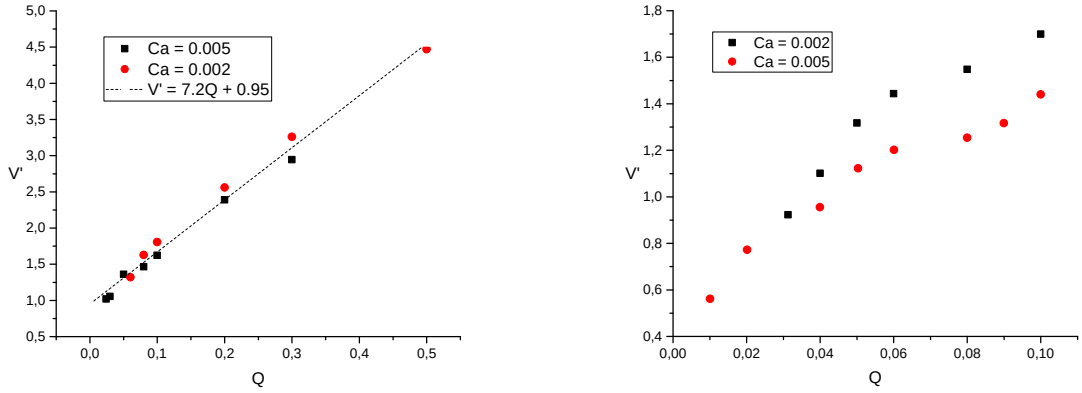

(a) Γ = 0.335

(b) Γ = 0.176

Figure 4.3: Variation of the droplet dimensionless volume V' with the flowrate ratio Q, at constant Ca in the squeezing regime for both geometries.

soon it reaches the T-junction. This causes the thread to rupture more rapidly, creating smaller droplets in a high formation frequency. The dispersed phase finger, downstream the inlet channel, is also visualized to be inclined relative to the walls, being more pronounced as Q decreases. This is particularly noticeable in the T3 geometry and it is due to large velocity difference between phases that causes the continuous phase to penetrate into the inlet channel. Droplet formation can be viewed as a balance between the interfacial tension force holding the interface from detaching and the tangential forces acting on it and originating from the velocity gradients existing between the continuous and dispersed phases. The

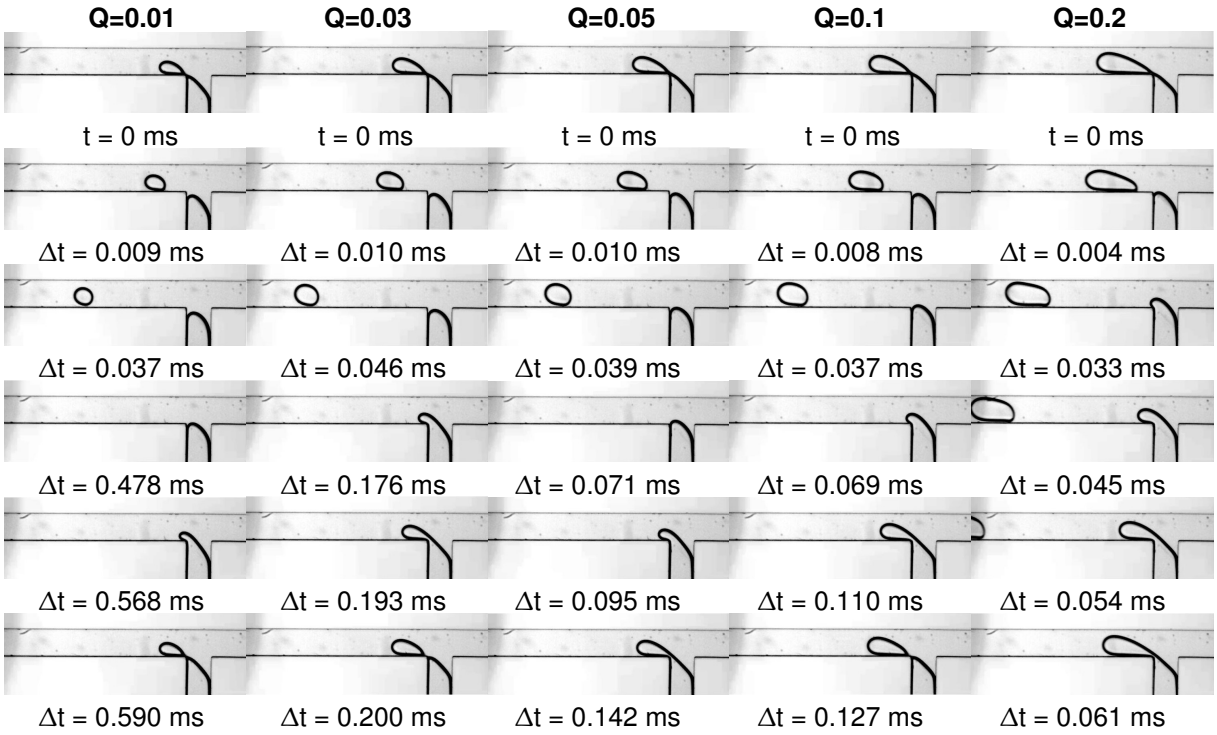

Figure 4.4: Droplet formation process in the dripping regime for Q = 0.01, 0.03, 0.05, 0.1 and 0.2, at Ca = 0.1, for the T1 geometry.

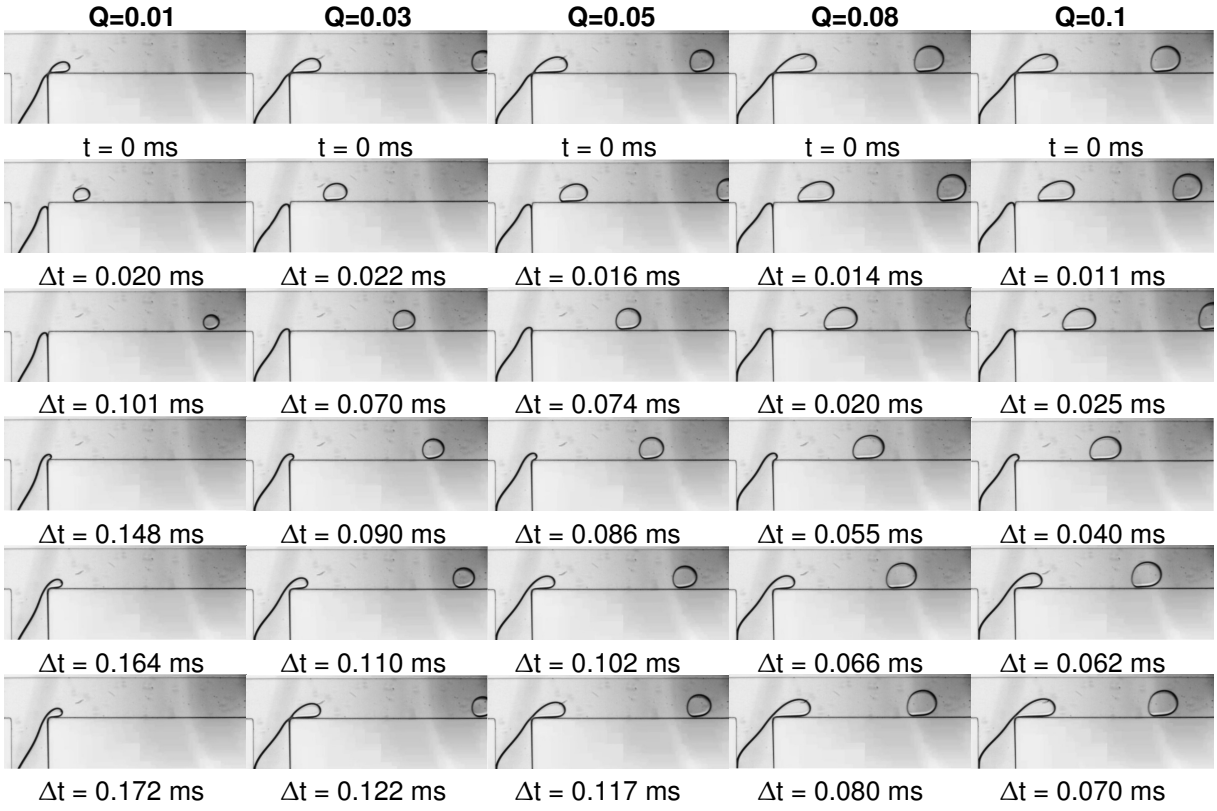

Figure 4.5: Droplet formation process in the dripping regime for Q = 0.01, 0.03, 0.05, 0.08 and 0.1, at Ca = 0.1, for the T3 geometry.

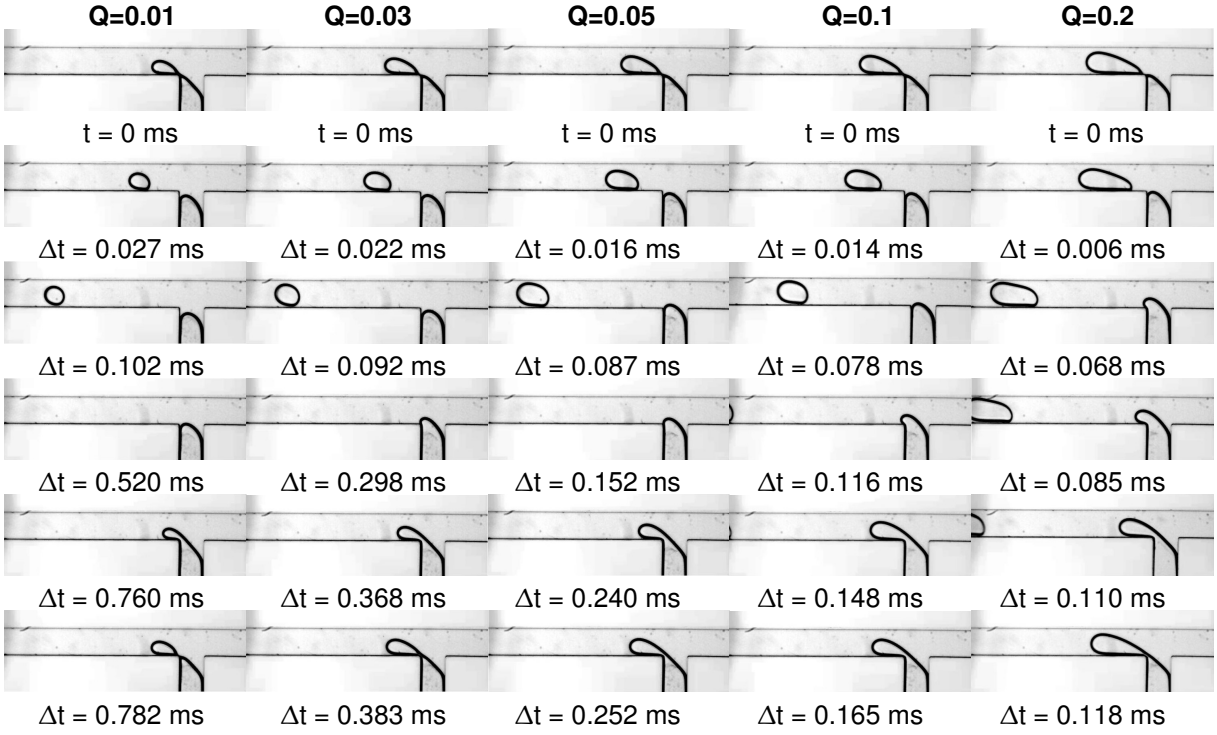

Figure 4.6: Droplet formation process in the dripping regime for Q = 0.01, 0.03, 0.05, 0.1 and 0.2, at Ca = 0.05, for the T1 geometry.

droplet reaches a critical size when the pressure difference due to the thread curvature cannot sustain any longer, which makes the droplet to detach.

The increase of V' with Q, in this regime, is less pronounced than that of the squeezing regime, as shown in the figure 4.8. From these observations, and in accordance to the literature, this regime is highly dependent on the Ca. In the dripping regime, a power-law was observed to be the best fitting for the data obtained. The results for the power-laws are displayed in the table 4.3.

Table 4.3: Power-law fitting (V' = K$\times$Q^m) parameters measured for the droplet volumes in the dripping regime for the T1 geometry.

Ca	K	m	R^2
0.1	2.35	0.44	0.9987
0.07	2.34	0.39	0.9813
0.05	2.36	0.42	0.9904

Further increase of Ca, the droplet formation will eventually attain the jetting regime, as observed in figure 4.9. In this regime, the dispersed phase interface invades part of the main channel and the formation of a stable jet verified for all the conditions tested. Furthermore, increasing the flowrate ratio Q caused the droplet detachment point to move downstream the T-junction, while the variation of V' with Q seems to recuperate a linear relation with a coefficient of determination R^2=0.9701 and a small coefficient of proportionality closer to one, as shown in figure 4.10.

Although researchers discuss about a critical Ca for regime change between squeezing, dripping and jetting, the evolution between the first two is gradual and a transitional regime is usually verified. In fact,

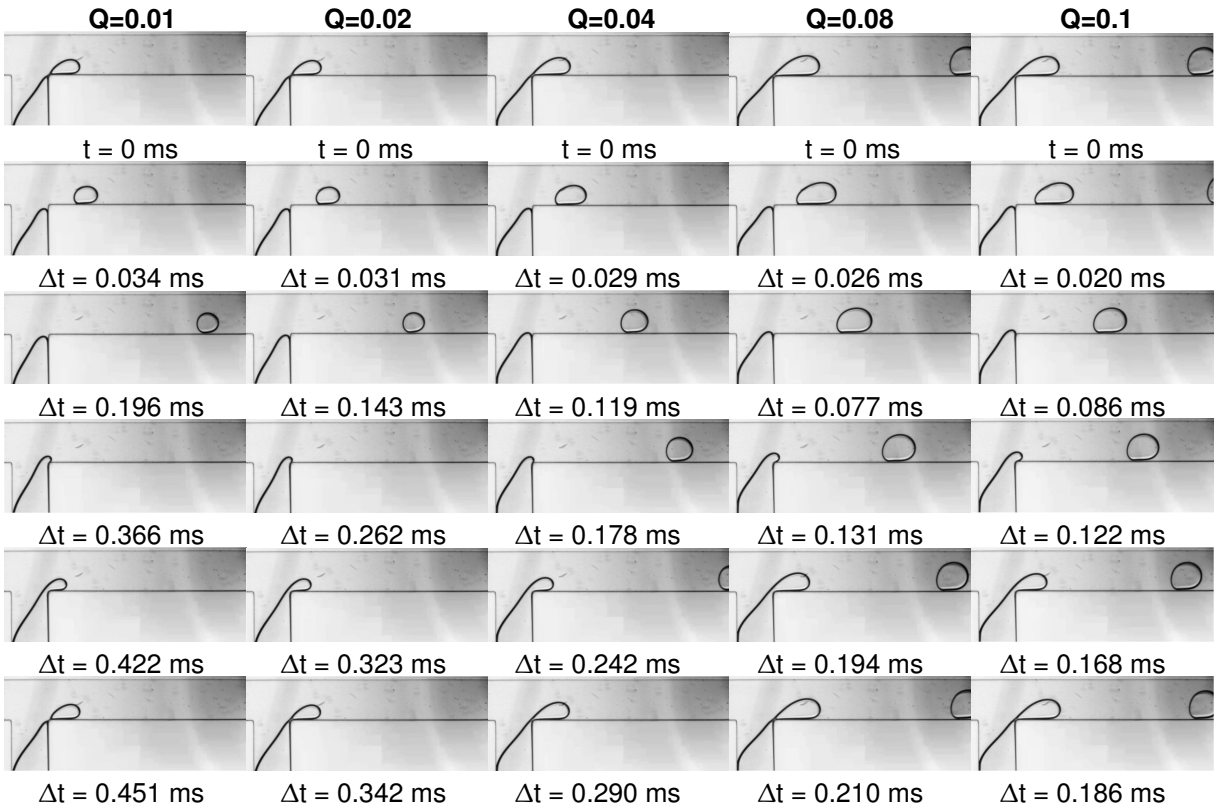

Figure 4.7: Droplet formation process in the dripping regime for Q = 0.01, 0.02, 0.04, 0.08 and 0.1, at Ca = 0.05, for the T3 geometry.

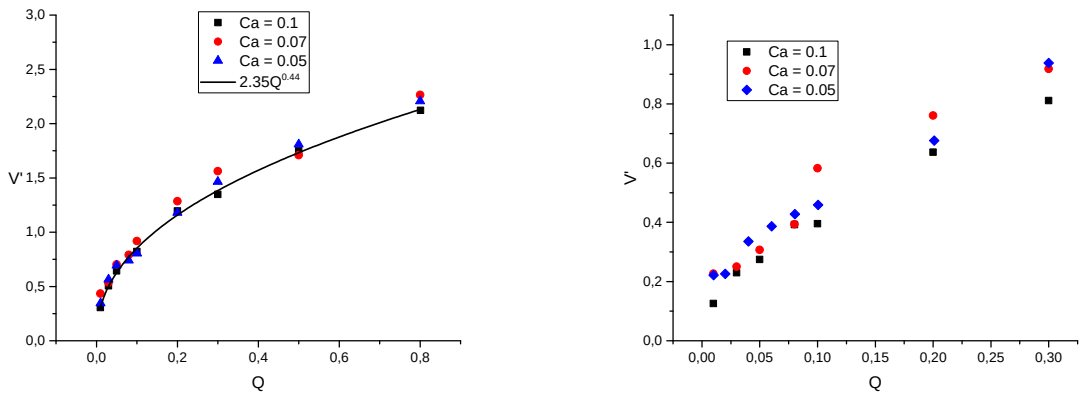

(a) Γ = 0.335

(b) Γ = 0.176

Figure 4.8: Variation of the droplet dimensionless volume V' with the flowrate ratio Q, at constant Ca in the dripping regime for both geometries.

even though the continuous phase flowrate Q_c is seen to have a dominant effect on droplet formation regimes, it is possible to verify a change in the formation phenomenon and, consequently, regime, by changing other parameters, such as the flowrate ratio [29]. In this work, the transitional regime was verified for $0.008 \leq \text{Ca} \leq 0.02$. For Q = 0.01, the dispersed phase interface is observed to grow and distort so that the main channel is not fully obstructed by it. However, its size is sufficient enough to also feel the effect of confinement, so a competition of break-up forces are in play. When the flowrate ratio

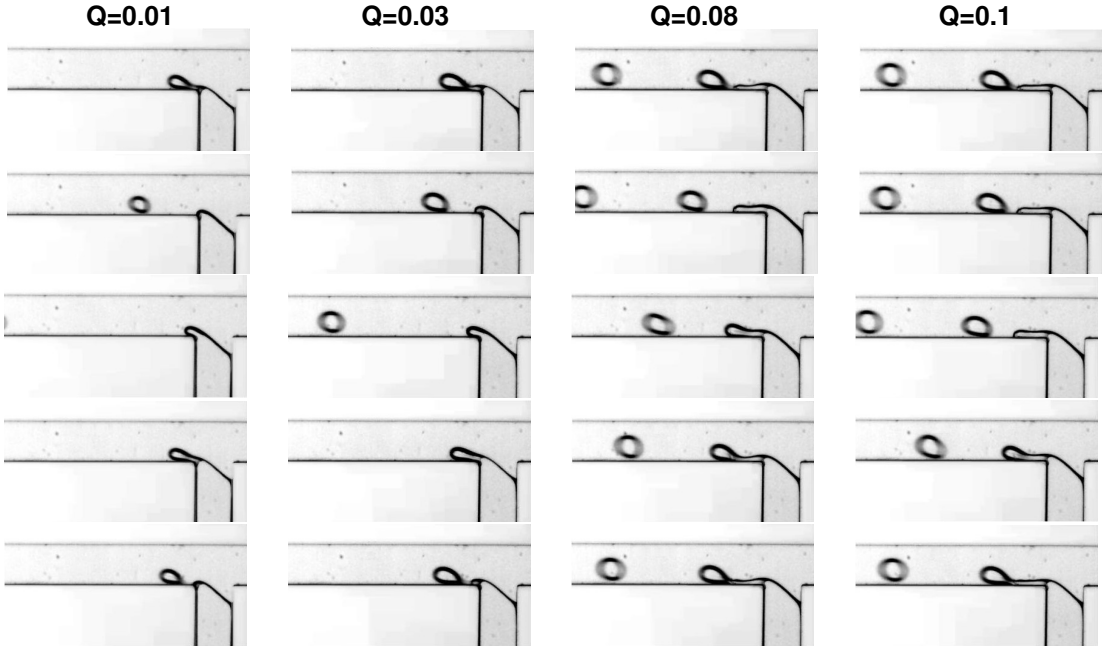

Figure 4.9: Droplet formation process in the jetting regime for Q = 0.01, 0.03, 0.08 and 0.1, at Ca = 0.3, for the T1 geometry.

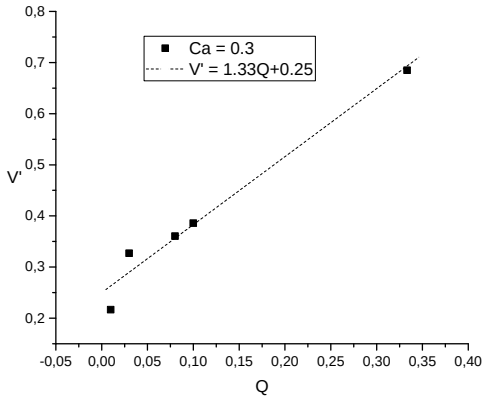

Figure 4.10: Variation of the dimensionless droplet volume V' as a function of the flowrate ratio Q in the jetting regime, at Ca = 0.3.

Q is increased, the thread growth starts to overcome the distortion of the interface at the T-junction and the thread is observed to fully occupy the channel width for Q = 0.2 in the T1 geometry, while for the T3 geometry it does not end up occupying it, entirely, as it can be observed in figures 4.11 and 4.12. This means again a restriction in the continuous phase flow and an increase of the pressure upstream. The change in detachment phenonema can almost be checked in figure 4.13 by the dashed line at Q = 0.1 drawn in the T1 geometry plot and a slight change in slope. Regarding the T3 geometry, this behaviour can be observed at $Q > 0.04$ for Ca = 0.02, while it is not noticeable for lower Ca.

The effect of the flowrate ratio Q on droplet formation times (or droplet formation frequency) is also studied, for constant Ca. Droplet formation times (DFT) bigger than 7 seconds were not measured since they surpassed the camera recording memory. The results, for both geometries, are plotted in a

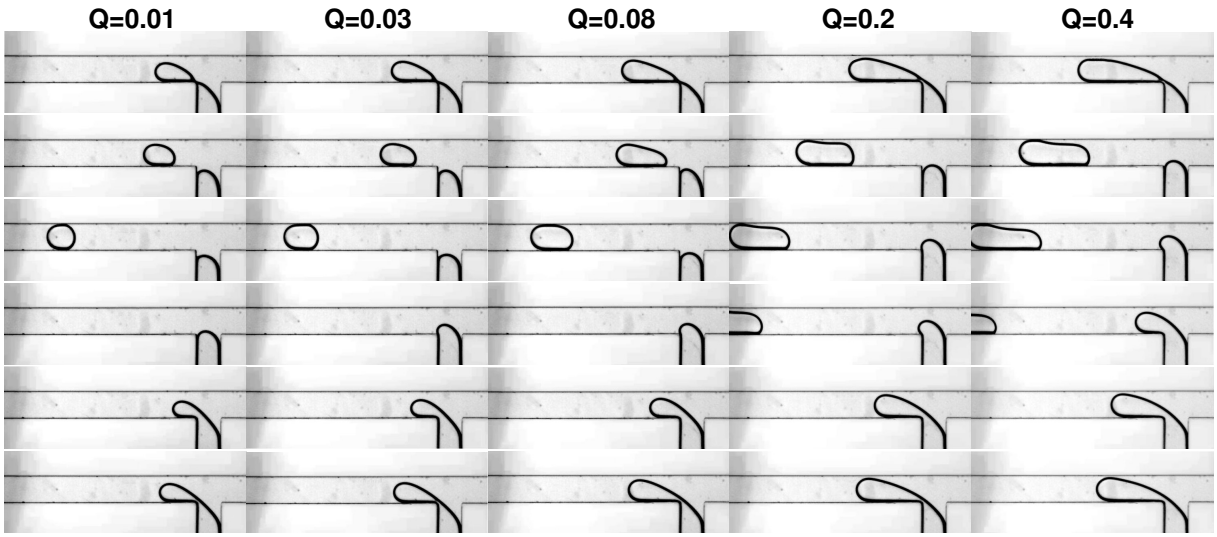

Figure 4.11: Droplet formation process in the transitional regime for Q = 0.01, 0.03, 0.08, 0.2 and 0.4, at Ca = 0.01, for the T1 geometry.

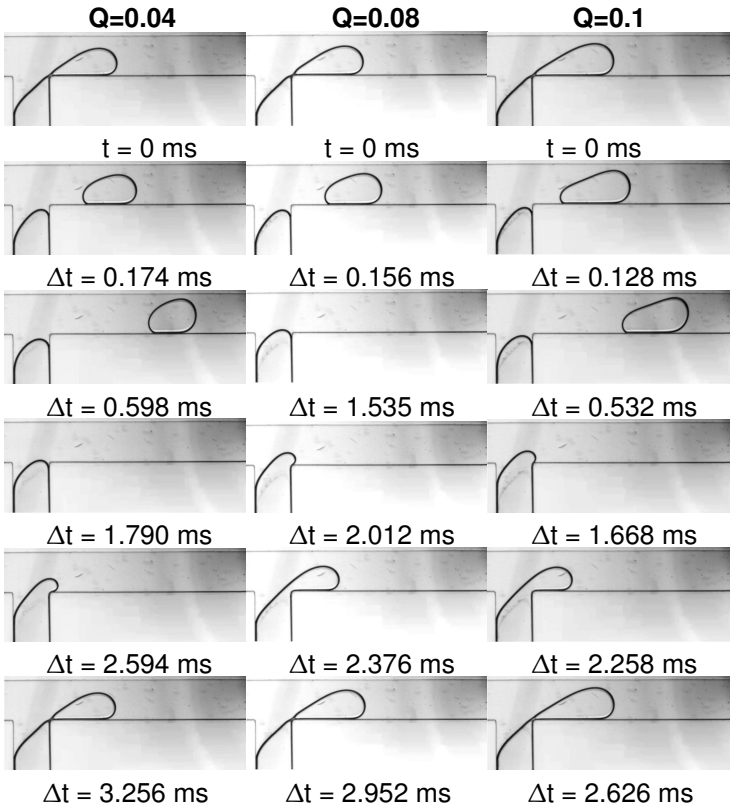

Figure 4.12: Droplet formation process in the transitional regime for Q = 0.04, 0.08 and 0.1, at Ca = 0.01, for the T3 geometry.

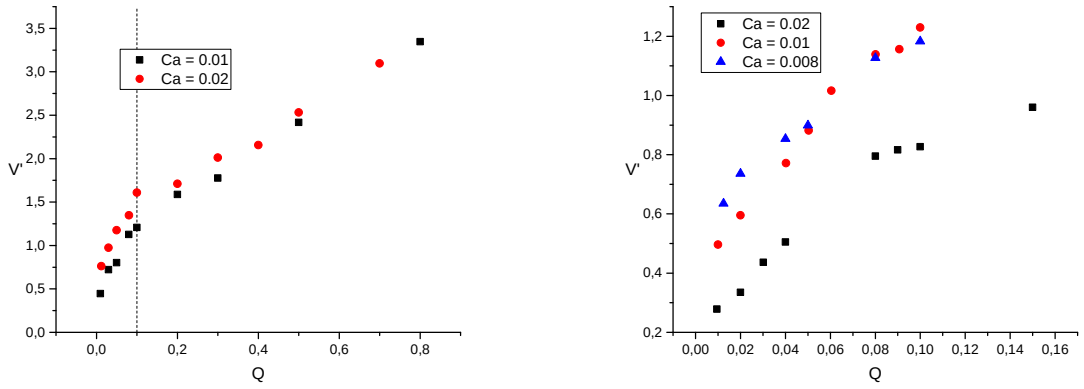

(a) Γ = 0.335 (b) Γ = 0.176

Figure 4.13: Variation of the dimensionless droplet volume V' as a function of the flowrate ratio Q in the transitional regime, for different Ca and for both geometries.

logarithmic scale graph in figure 4.14.

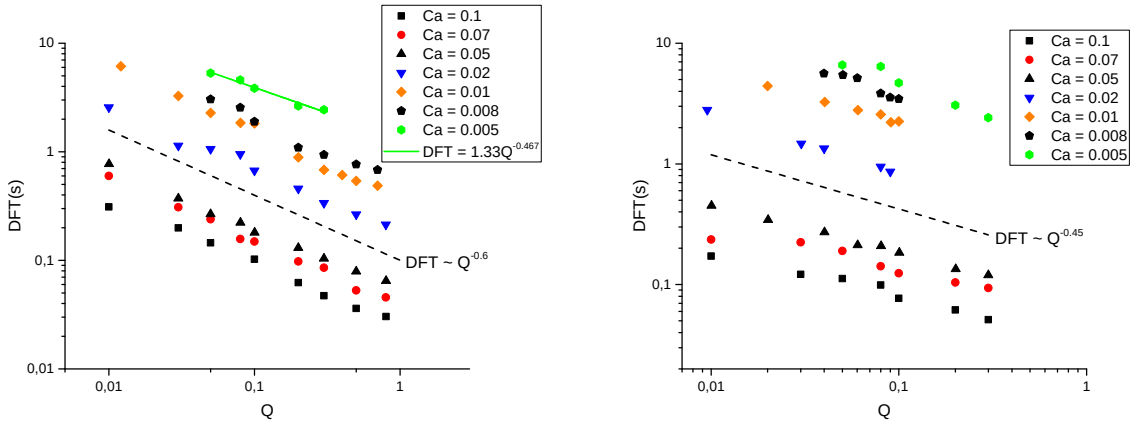

(a) Γ = 0.335 (b) Γ = 0.176

Figure 4.14: Variation of droplet formation time (DFT) as a function of the flowrate ratio Q, for different Ca and for both geometries.

From the results, it is noted that the droplet formation time decreases as the dispersed phase flowrate Q_d is increased, for most of the conditions. For all Ca numbers tested, a power-law dependence of the type DFT = KQ^m is verified. In the dripping regime, for the T1 geometry, the power exponent value m of -0.6 was noted to be almost constant, with a maximum difference of 5.87 $\%$. However, an increase in the constant coefficient K is observed as the Ca number is decreased. Furthermore, for Ca = 0.005, a deviation to the previous power-law trend is notorious, most likely due to a change in regime. The fitting is adjusted towards a lower absolute value of the exponent, represented in the plot by the solid line, indicating a smaller dependence on the Ca, appropriate for the squeezing regime. For the T3 geometry, a different power-law exponent is also obtained. In the dripping regime, the data seems to agree well with DFT(s) $\propto Q^{-0.45}$. This change in the the exponent indicates that at lower Γ, there is a smaller effect of the flowrate ratio Q on droplet formation time, and, therefore, V'.

According to the models previously tested, there seems to exist an agreement with the different droplet formation regimes and the transition from squeezing to dripping can be identified by a change of the effect of DFT with Q. Furthermore, the aspect ratio influenced DFT by a smaller absolute value of the exponent.

As it was mentioned in section 3.3, the calculation of the droplet volume was performed using equation 3.1, valid for most of the conditions of this work. The theoretical values obtained from the pump were compared with the calculated ones by plotting both dispersed phase flowrates, as depicted in figure 4.15

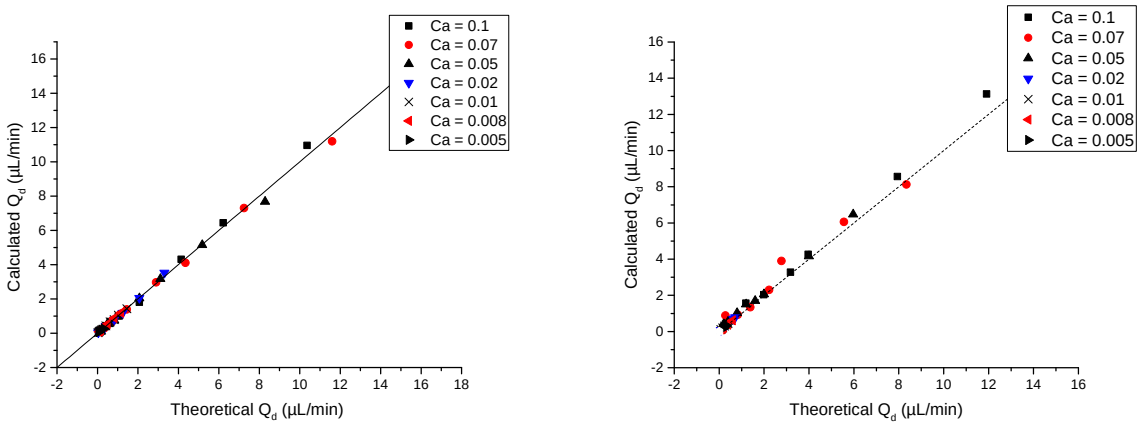

(a) Γ = 0.335

(b) Γ = 0.176

Figure 4.15: Comparison of the theoretical and experimental (by means of equation 3.1) dispersed phase flowrates calculated for both geometries and for all conditions.

A very good agreement of the data for the T1 geometry is achieved, whereas for the T3 geometry some minor data points are not well correlated. This is most likely due to an irregular droplet shape generation that leads to volume calculation errors. It was also observed that the polydispersity α values were highly dependent on the Capillary number. For Ca $>$ 0.05, α was not higher than 3 %. For lower Ca, this value reached a maximum of 12 % for Ca = 0.002 and Q = 0.3.

4.1.2 Influence of the Capillary number Ca

The influence of the Ca on droplet volume was studied by maintaining a constant flowrate ratio Q and a constant dispersed phase flowrate Q_d. Experimentally, this meant varying both flowrates accordingly for the former case and varying just the continuous phase flowrate Q_c for the latter. The results are plotted in figures 4.16 and 4.17.

The droplet V' was found to decrease with Ca for most of the flowrate ratios tested and a power-law behaviour is verified for both geometries. The exponent seems not to vary much for the T1 geometry, while for the T3 geometry, a change in slope is observed for Ca = 0.01 accompanied by a change in the exponent of the power law, which is not clearly observed in the T1 geometry. Furthermore, the change in the fitting coefficient from V' $\propto$ Ca$^{-0.25}$ to V' $\propto$ Ca$^{-0.45}$ shows that Ca is a more influential parameter in the dripping regime as it has a more steeper decreasing change, whereas in the T1 geometry, the effect of confinement is more dominant and the Ca influence is not so clear. One has also to take into

account that the low aspect ratio might also influence this effect, since there is a constant confinement in the height direction for most of the conditions studied.

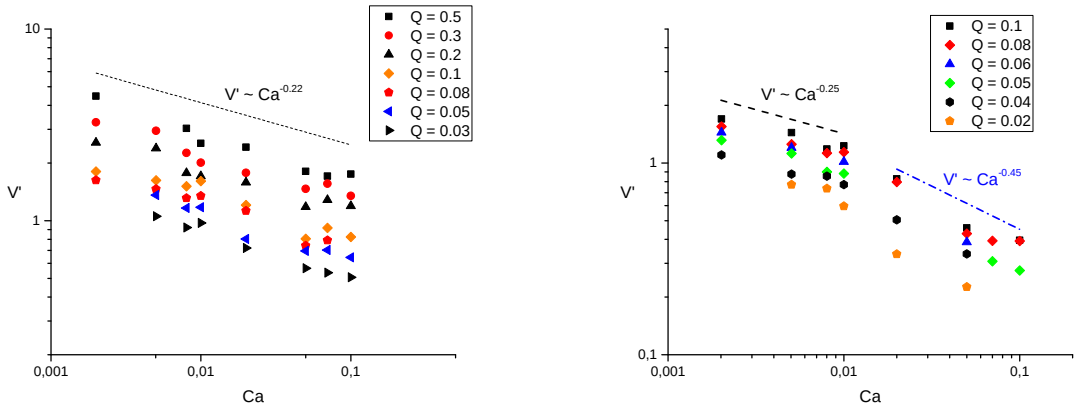

(a) Γ = 0.335 (b) Γ = 0.176

Figure 4.16: Variation of the dimensionless droplet volume V' with Ca for different Q and for both geometries.

When the effect of the dispersed phase flowrate Q_d is considered in figure 4.17, it is observed that this parameter has a much more strong influence on the droplet V' than the flowrate ratio Q. The exponential fitting parameter is increased (in absolute terms) to -0.62.

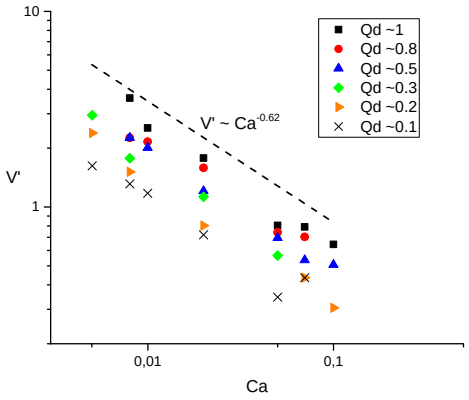

Figure 4.17: Variation of the dimensionless droplet volume V' with Ca for different Q_d and T1 geometry.

4.1.3 Influence of the aspect ratio

In this section, the influence of the aspect ratio will be assessed for the different droplet formation regimes. The data for the different formation regimes are plotted separately in figure 4.18.

The plots reveal that the size of the droplets formed decreases as the aspect ratio Γ decreases. For the dripping regime, a clear deviation of the results for the two different aspect ratios is observed and this difference is seen to increase with the flowrate ratio Q. However, a similar behaviour with Q is verified. The decrease in Γ while keeping the same width ratio Λ is expected to affect the shear forces acting

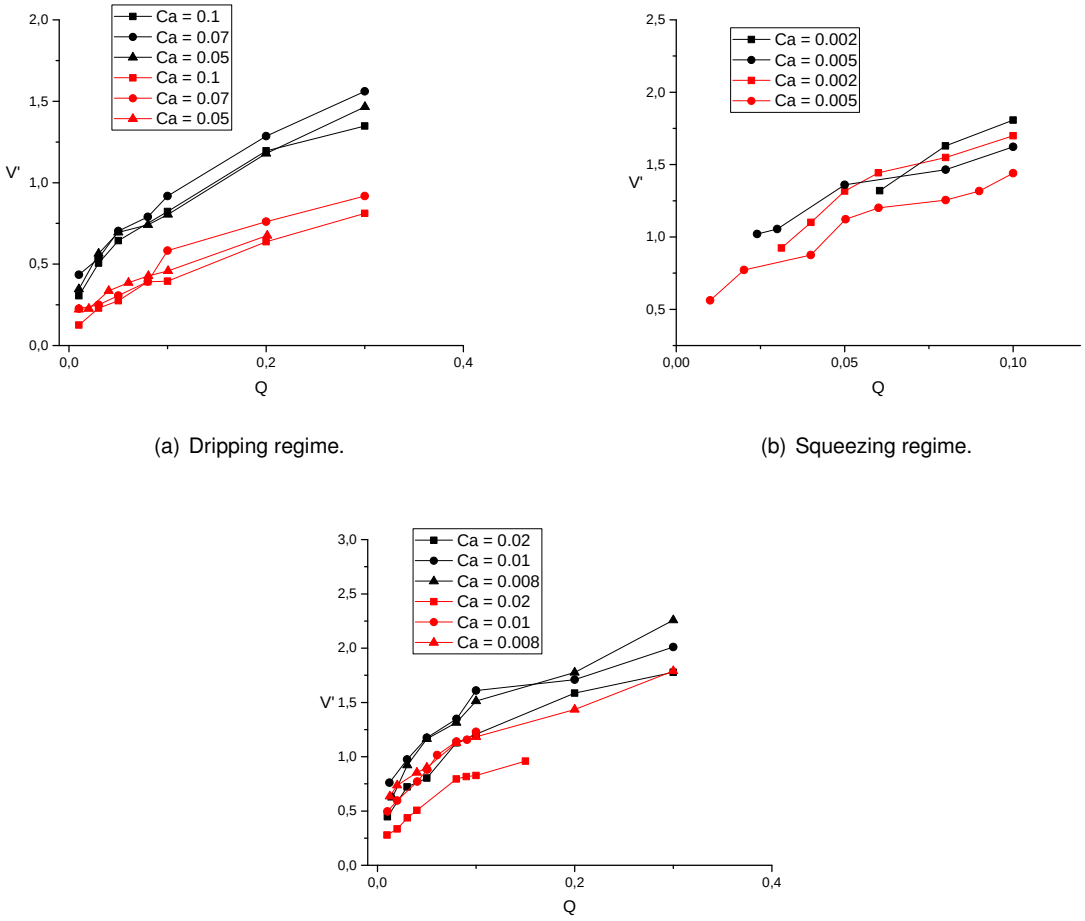

(a) Dripping regime.

(b) Squeezing regime.

(c) Transition regime.

Figure 4.18: Variation of the dimensionless droplet volume V' as a function Ca, for different Q_d. The black points refer to the T1 geometry (Γ = 0.335) while the red points refer to the T3 geometry (Γ = 0.176).

on the emerging thread, with smaller velocity gradients at the interface in the beginning of the growth stage. So, the dispersed phase thread grows in a smaller time interval, which leads to a faster necking stage and smaller V'. It also explains two behaviours observed: why the flowrate ratio Q has an higher effect in droplets formed in the dripping regime than in the squeezing and transitional ones; and why this effect seems to increase for higher Q values in the dripping regime. However, in the squeezing regime, since the confinement effect is the dominant phenomenon, this process is not so evident. Therefore, for the squeezing regime, the observed non-dimensional droplet volumes are similar for both Ca numbers and with a comparable growing behaviour. For the transition regime, since both forces share similar importance in the process, this physical description is also not so clear but similar comparisons are checked. It is therefore concluded that a low aspect ratio Γ does have a strong impact on the droplet size and it should be taken into account, specially for high Ca numbers.

4.2 Aqueous Al_2O_3 nanofluid droplet formation

The influence of the addition of nanoparticles to the dispersed phase base fluid of DIW with 0.05 % w/w fluorescent dye will be studied and presented in this section. Three different volume $\%$ concentrations of Al_2O_3 nanoparticles - see table 4.2 - were added and tested in the T1 geometry, for the same conditions of flowrate ratio Q and continuous phase flowrate Q_c, corresponding to dripping and transition regimes. Data obtained will be compared and the evaluation of Q, Ca and vol. % of Al_2O_3 parameters on droplet size analyzed.

4.2.1 Influence of the flowrate ratio Q and Capillary number Ca

Following the experimental procedure of subsection 4.1.1, the influence of the flowrate ratio Q on droplet formation is investigated for the T1 geometry and four different Ca conditions. Both continuous and dispersed phase flowrates Q_c and Q_d were maintained equal to the ones from section 4.1 for DIW and 0.05 % w/w fluorescent dye. The data obtained is also compared to one from previous section for DIW and it is identified by 0% Al_2O_3 in the plots below - see figures 4.19. For this work, small % in volume of Al_2O_3 are applied to the base fluid in order to avoid clogging of the microchannels and agglomeration during flow.

Because the flowrates Q_c and Q_d were kept the same, different droplet volumes are expected since there is a non negligible variation of fluid properties affecting droplet formation. The interfacial tension between phases and the viscosity were found to increase with the addition of Al_2O_3 nanoparticles, as seen in section 2.2 - Figures 2.14 and 2.17. Besides these two properties sharing distinct effects on droplet formation, they also share different importance, depending on the regime, as it was extensively discussed during the previous analysis and also in the literature.

In figure 4.19, the dimensionless droplet volumes V' are plotted against Q, for constant Ca of the continuous phase.

From the results data, at Ca = 0.1 (Figure 4.19 (a)), it is not observed a notorious deviation of the values of V' relative to the base fluid ones (0% Al_2O_3). The non-dimensional droplet volumes, for 0.1% concentration of Al_2O_3, are observed to match closely to the ones for DIW, while, for the lower concentrations, it seems to slightly reduce in comparison with the previous two. However, for smaller values of the continuous phase Ca, specifically Ca = 0.02 (Figure 4.19 (c)) and Ca = 0.01 (Figure 4.19 (d)), V' increases with the concentration of Al_2O_3 nanoparticles for most of the conditions. The maximum increase of V' in comparison with the value from the base fluid was obtained for Ca = 0.01, a concentration of 0.1% and Q = 0.01, as 38%. This specific condition of Q = 0.01 is also noted to be the one where the maximum deviation of V', concerning the concentration values and comparing to the base fluid ones, occurs. For Ca = 0.05 (Figure 4.19 (b)), the values of V' are in a intermediate region in between, since the values for 0.01% and 0.025% match the values of 0% concentration of Al_2O_3, while the volumes for 0.1% are already higher.

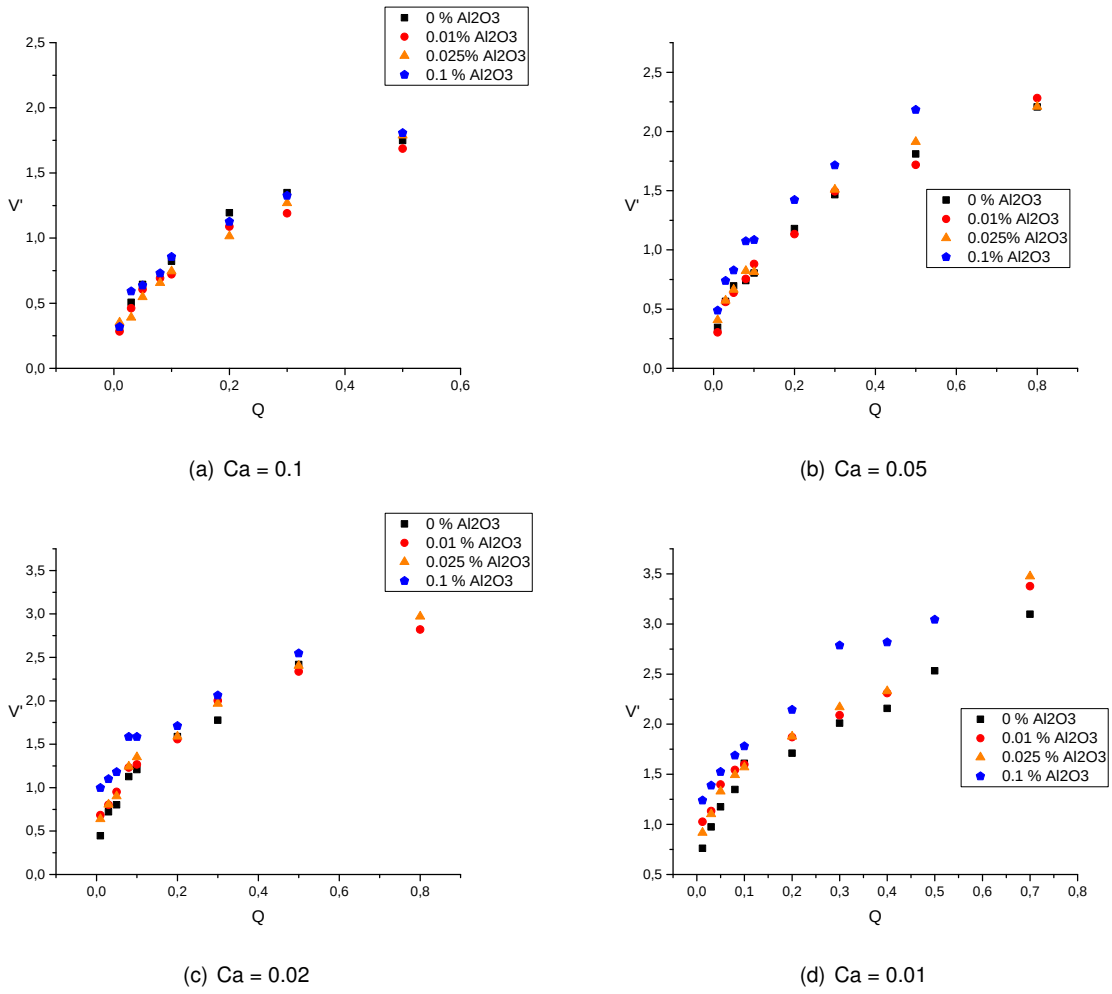

Figure 4.19: Variation of the dimensionless droplet volume V' as a function of the flowrate ratio Q, for different vol. $\%$ of nanoparticles in the dispersed phase and for different Ca.

4.2.2 Influence of the concentration of Al_2O_3 nanoparticles

From the previous section, it was noted that, as the Ca number is increased, the influence of the addition of Al_2O_3 nanoparticles is noted to decrease, and the difference comparatively to the values obtained in section 4.1 shortens. This can easily be visualized if we plot the variation of V' with the different concentration of nanoparticles, as it is shown in figure 4.20.

The non-dimensional droplet volumes, for Ca = 0.01 and Ca = 0.02, display a growing variation with the addition of Al_2O_3 nanoparticles, for most of the cases. However, for Ca = 0.05, this trend is not strictly observed while for Ca = 0.1, the values of V' actually slightly reduce.

From this analysis, it is plausible to argue that distinct phenomenon must be at play for the several Ca conditions, similarly to what was discussed in section 4.1, and that influences nanofluid droplet volume differently.

The increase of the viscosity ratio (by means of an increase of the dispersed phase viscosity μ_d), with the addition of nanoparticles, is expected to influence droplet V' by affecting the shear forces exerted at the thread interface. Therefore, for a larger viscosity ratio $\lambda = \frac{\mu_d}{\mu_c}$ (where the subscripts c and d mean continuous and dispersed phases, respectively), a lower shear force at the interface is expected.

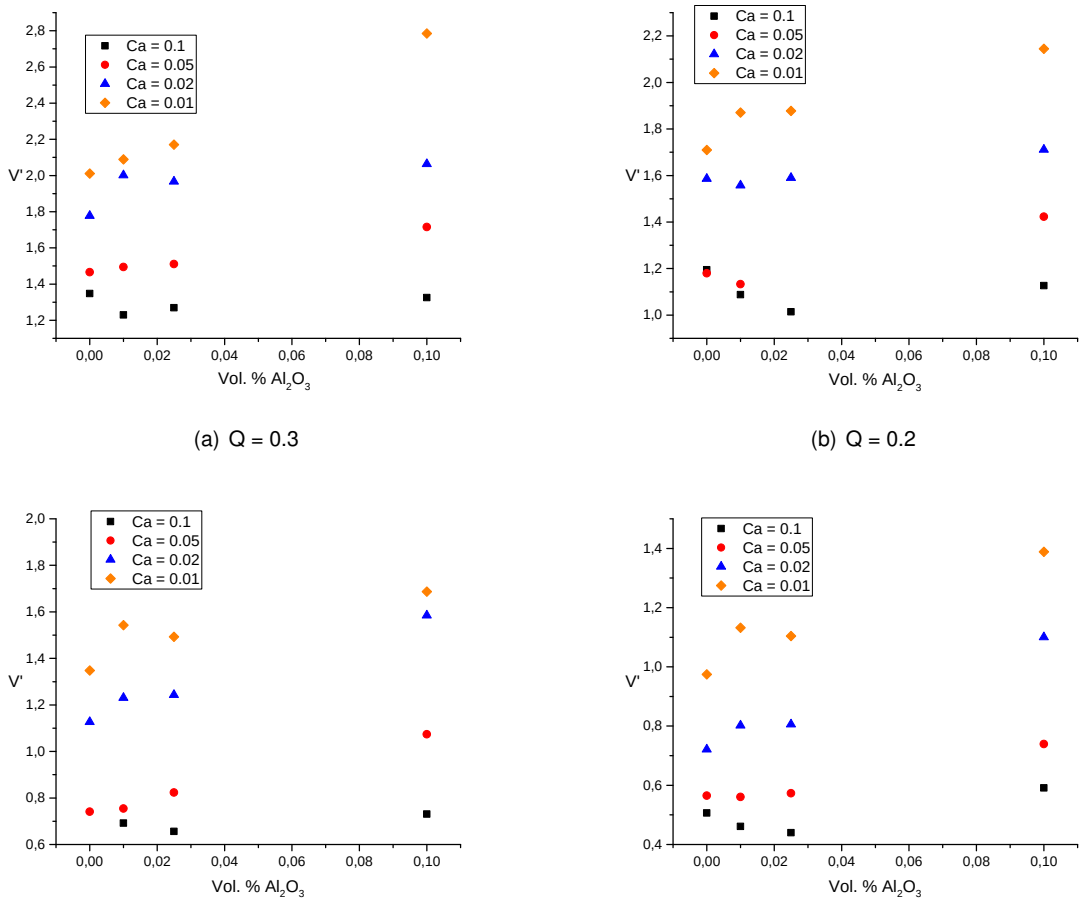

Figure 4.20: Variation of the dimensionless droplet volume V' as a function of vol. $\%$ concentration of nanoparticles in the dispersed phase, for constant Q and for different Ca.

However, the effect of μ_d is expected to be negligible when compared with the one from μ_c, that remains constant and much greater than the former. Furthermore, an increase in μ_d is also added in terms of the friction resistance at the disperse phase fluid thread, that opposes the shear and pressure break-up forces. Stronger streamwise forces will then be required to push the same volume of dispersed phase fluid. This has similar implications as the increase of the interfacial tension with nanoparticle concentration, because this leads to a stronger interface, less prone to detachment. These remarks might explain why the values of V' for the dripping regime, at Ca = 0.1, do not differ much with the addition of nanoparticles, while the values for the transitional regime, specially at Ca = 0.01, notoriously increase comparatively to the ones obtained for DIW.

The trend of the results appears to show that the reduction of Ca makes the V' variation with the % concentration of Al_2O_3 to be more pronounced. Furthermore, it seems that there is a critical Ca above which the droplet volume V' can be altered and become smaller than the one from base fluid DIW conditions. Nonetheless, such critical Ca is not obvious and it depends on the % concentration of nanoparticles and various factors like geometry and dimensions of channels as well as types of dispersed and continuous phases, an issue that clearly requires much more experiments to be analyzed.

Apart from the changes in the physical properties for the nanofluids, no other justification could be made for such observations regarding droplet volume. The results obtained in this section are of first kind for Al_2O_3 aqueous nanofluid in a microfluidic T-junction, thus comparisons of the results obtained are not possible.

Chapter 5

Conclusions and Future Work

5.1 Conclusions

A strong research has been done up to now on several microfluidic droplet generators, specially for T-junction geometries. However, the application of nanofluids in these devices has not received much attention so far and only a handful of studies were performed by a specific group [39-42]. The data obtained from various researchers show some discrepancies, mainly due to the excessive number of influencing variables (*i.e.* experimental parameters) that can affect such type of tests, such as fluids used, flowrates, materials, geometries, etc. Furthermore, the acquisition of the data requires several assumptions to be made, besides the difficulty of performing the experiments themselves. This makes droplet formation studies a very hard task and, in spite of the already formalized incipient theory, a great deal of research work still needs to be done to fully understand droplet formation dynamics, nanoparticles flow behaviour, and the coupling between the two.

In this context, two T-shaped microchannels were manufactured by soft lithography techniques, with the same width ratio equal to 1 and aspect ratios of 0.375 (T1 geometry) and 0.1875 (T3 geometry). To acquire the images, a CMOS camera was mounted on a microscope and the digital images were acquired and saved to be post-processed, to retrieve data for analysis.

A thorough analysis of distilled water droplet formation characteristics was performed by employing 8 diferent Ca (0.002-0.1) and flowrate ratios Q (0.01-0.8) conditions for both geometries. Furthermore, the application of different concentrations of Al_2O_3 to the base DIW dispersed phase was carried out. This included its properties characterization, their contributional link to droplet formation and size and the comparison of the data for the case without nanofluids.

The different phenomena governing the formation process for each regime were analyzed. The squeezing regime, occurring for Ca $\leq$ 0.005, was found to be strongly dependent on the flowrate ratio, and a linear fitting proved to represent the data accurately for the T1 geometry. The formed droplets filled the entire channel and the increased pressure upstream the dispersed phase thread was found to be the dominant mechanism of detachment process, through the resulting strong favourable pressure gradient across the fluids interface. With the increase of the Ca, the transitional regime was attained, which is

characterized by the fact that shear forces become as relevant as the pressure forces in the detachment process. The non-dimensional droplet volume V' is expected to dependent on both Q and Ca in this regime and droplet volume predictions are difficult. At Ca $\geq$ 0.05, dripping regime was achieved. This regime was observed to be more dependent on the Ca than the two other regimes. Formed droplets showed minor variations in V' with Q and were accurately fitted to a power-law behaviour. These trends were attributed to the dominating shear stress mechanism of detachment. The variation of V' with Ca was studied for constant flowrate ratios and for constant dispersed phase flowrate Q_d, the latter only for the T1 geometry. It was observed a decrease of V' with Ca, for all regimes and most of the Q values tested. A higher dependence of V' on Ca was observed with constant dispersed phase flowrate Q_d, with a fitted power-law representing accurately the data for an exponent of -0.62. Finally, it was also studied the influence of the geometry by changing the aspect ratio. Droplet non-dimensional volume V' decreased with the aspect ratio. This behaviour was attributed to the decreasing shear stress gradients as the widths of dispersed and continuous phase channels are increased, leading to faster growth times. Furthermore, this effect was observed to be more pronounced in the dripping regime.

To complement this study, the Ca for jetting regime was also determined experimentally, and its value is 0.3 for the T1 geometry. This regime is characterized by the formation of a stable jet where droplet detachment occurs downstream the main channel and this detachement station was observed to move downstream as the flowrate ratio Q increased. A linear fitting proved to fit the data with reasonable accuracy, as V' increases with Q smoothly.

The addition of Al_2O_3 nanoparticles to the distilled water phase in the droplet generator was observed to promote an increase of V' in the transitional regime, whereas for the dripping regime the influence is negligible as the data practically coincide for the different studied concentrations. This was attributed to the change of properties, since it was observed that both interfacial tension and viscosity increased with % of Al_2O_3 nanoparticles. This change in the physical properties of the dispersed phase was more noticeable at lower Ca due to the increased pressure upstream gaining importance in the break-up process. Furthermore, a similar trend of the increase of V' with the flowrate ratio, with and without nanoparticles, was observed.

At the end of this work, a successful utilization of nanofluids in microchannel devices and as dispersed phase fluid for the formation of monodisperse droplets was obtained. Care should be taken since the application of nanoparticles in microchannels were observed to clog the microfluidic device. This topic still requires further studies as applications of nanofluids for micro-sized flow channels and devices have promissing future in important applications and it's the wish of the author that it opens extents for future work.

5.2 Future Work

For future work, it is suggested the continuation of a study of the application of nanofluids in droplet based microfluidics. It would be interesting to study the influence on the application of different types of nanoparticles, regarding size, type and also shape, specially not spherical ones.

It is also proposed a numerical approach to simulate the formation of droplets dynamics, which would allow for the detailed knowledge of the velocity and pressure fields, since these are difficult to obtain experimentally without compromising the retrieval of accurate results. Moreover, it can also complement the experimental data obtained for this thesis.

Finally, the application of experimental techniques such as μ-PIV for the study of velocity field can also some provide insights into the characterization of the relevant phenomena at stake, governing droplet generation.

References

[1] H. Gu, M. H. Duits, and F. Mugele. Droplets formation and merging in two-phase flow microfluidics. *International Journal Of Molecular Sciences*, 12(4):2572–2597, 2011. ISSN 14220067. doi: 10.3390/ijms12042572.

[2] R. Seemann, M. Brinkmann, T. Pfohl, and S. Herminghaus. Droplet based microfluidics. *Reports on Progress in Physics*, 75:1–41, 2012. ISSN 10643745. doi: 10.1007/978-1-62703-134-9_15.

[3] N.-T. Nguyen and S. T. Wereley. *Fundamentals and Applications of Microfluidics*. 2nd edition, 2006. ISBN 9781580539722.

[4] A. Manz, N. Graber, and H. M. Widmer. Miniaturized total chemical analysis systems: a novel concept for chemical sensing. *Sensors And Actuators B: Chemical*, 1:244–248, 1990. ISSN 01628828. doi: 10.1109/34.387509.

[5] G. T. Vladisavljević, N. Khalid, M. A. Neves, T. Kuroiwa, M. Nakajima, K. Uemura, S. Ichikawa, and I. Kobayashi. Industrial lab-on-a-chip: Design, applications and scale-up for drug discovery and delivery. *Advanced Drug Delivery Reviews*, 65(11-12):1626–1663, 2013. ISSN 0169409X. doi: 10.1016/j.addr.2013.07.017.

[6] Hue P. Le. Progress and Trends in Ink-jet Printing Technology. *Journal of Imaging Science and Technology*, 42(1):49–62, 1998.

[7] J. Strutt and L. Rayleigh. On the instability of jets. *Proceedings of the London mathematical society*, 1:4–13, 1878. doi: https://doi.org/10.1112/plms/s1-10.1.4.

[8] W. L. Chou, P. Y. Lee, C. L. Yang, W. Y. Huang, and Y. S. Lin. Recent advances in applications of droplet microfluidics. *Micromachines*, 6(9):1249–1271, 2015. ISSN 2072666X. doi: 10.3390/mi6091249.

[9] L. I. U. Zhao-miao, Y. Yang, D. U. Yu, and P. Yan. Advances in droplet-based microfluidic technology and its applications. *Chinese Journal of Analytical Chemistry*, 45(2):282–296, 2017. doi: 10.1016/S1872-2040(17)60994-0.

[10] S.-y. Teh, R. Lin, L.-h. Hung, and A. P. Lee. Droplet microfluidics. *Lab on a Chip*, 2(8):198–220, 2008. doi: 10.1039/b715524g.

[11] S. Vyawahare, A. D. Griffiths, and C. A. Merten. Miniaturization and parallelization of biological and chemical assays in microfluidic devices. *Chemistry and Biology*, 17(10):1052–1065, 2010. ISSN 10745521. doi: 10.1016/j.chembiol.2010.09.007.

[12] A. Choi, S. U. S.; Eastman. Enhancing thermal conductivity of fluids with nanoparticles. *Proceedings of the 1995 ASME International Mechanical Engineering Congress and Exposition*, 66(March): 99–105, 1995.

[13] S. Senapati, A. K. Mahanta, S. Kumar, and P. Maiti. Controlled drug delivery vehicles for cancer treatment and their performance. *Signal Transduction and Targeted Therapy*, 3(1):1–19, 2018. ISSN 20593635. doi: 10.1038/s41392-017-0004-3.

[14] S. K. Das, S. U. Choi, and H. E. Patel. Heat transfer in nanofluids - A review. *Heat Transfer Engineering*, 27(10):3–19, 2006. ISSN 01457632. doi: 10.1080/01457630600904593.

[15] H. Bruus. *Theoretical Microfluidics*. Oxford University Press, Oxford, 2008. ISBN 9788578110796. doi: 10.1017/CBO9781107415324.004.

[16] J. Hale. *The thermal fluctuations of red blood cells*. Number September. 2009.

[17] F. M. White. Fluid Mechanics (4th Edition). 2010. ISSN 1364-0321. doi: http://dx.doi.org/10.1016/j.rser.2004.09.010.

[18] C. N. Baroud, F. Gallaire, and R. Dangla. Dynamics of microfluidic droplets. *Lab on a Chip*, 10(16): 2032–2045, 2010. ISSN 14730189. doi: 10.1039/c001191f.

[19] G. F. Christopher and S. L. Anna. Microfluidic methods for generating continuous droplet streams. *Journal of Physics D: Applied Physics*, 40(19):319–336, 2007. ISSN 00223727. doi: 10.1088/0022-3727/40/19/R01.

[20] J. H. Xu, S. W. Li, J. Tan, Y. J. Wang, and G. S. Luo. Controllable preparation of monodisperse O/W and W/O emulsions in the same microfluidic device. *Langmuir*, 22(19):7943–7946, 2006. ISSN 07437463. doi: 10.1021/la0605743.

[21] T. Thorsen, R. W. Roberts, F. H. Arnold, and S. R. Quake. Dynamic pattern formation in a vesicle-generating microfluidic device. *Physical Review Letters*, 86(18):4163–4166, 2001. ISSN 00319007. doi: 10.1103/PhysRevLett.86.4163.

[22] P. Garstecki, M. J. Fuerstman, H. A. Stone, and G. M. Whitesides. Formation of droplets and bubbles in a microfluidic T-junction - Scaling and mechanism of break-up. *Lab on a Chip*, 6(3): 437–446, 2006. ISSN 14730189. doi: 10.1039/b510841a.

[23] G. F. Christopher, N. N. Noharuddin, J. A. Taylor, and S. L. Anna. Experimental observations of the squeezing-to-dripping transition in T-shaped microfluidic junctions. *Physical Review E - Statistical, Nonlinear, and Soft Matter Physics*, 78(3):1–12, 2008. ISSN 15393755. doi: 10.1103/PhysRevE.78.036317.

[24] J. H. Xu, S. W. Li, J. Tan, and G. S. Luo. Correlations of droplet formation in T-junction microfluidic devices: From squeezing to dripping. *Microfluidics and Nanofluidics*, 5(6):711–717, 2008. ISSN 16134982. doi: 10.1007/s10404-008-0306-4.

[25] A. R. Abate, A. Poitzsch, Y. Hwang, J. Lee, J. Czerwinska, and D. A. Weitz. Impact of inlet channel geometry on microfluidic drop formation. *Physical Review E - Statistical, Nonlinear, and Soft Matter Physics*, 80(2):1–5, 2009. ISSN 15393755. doi: 10.1103/PhysRevE.80.026310.

[26] V. Van Steijn, C. R. Kleijn, and M. T. Kreutzer. Predictive model for the size of bubbles and droplets created in microfluidic T-junctions. *Lab on a Chip*, 10(19):2513–2518, 2010. ISSN 14730189. doi: 10.1039/c002625e.

[27] T. Glawdel, C. Elbuken, and C. L. Ren. Droplet formation in microfluidic T-junction generators operating in the transitional regime. I. Experimental observations. *Physical Review E - Statistical, Nonlinear, and Soft Matter Physics*, 85(1):1–9, 2012. ISSN 15393755. doi: 10.1103/PhysRevE.85.016322.

[28] J. D. Wehking, M. Gabany, L. Chew, and R. Kumar. Effects of viscosity, interfacial tension, and flow geometry on droplet formation in a microfluidic T-junction. *Microfluidics and Nanofluidics*, 16(3):441–453, 2014. ISSN 16134990. doi: 10.1007/s10404-013-1239-0.

[29] K. Loizou, V.-L. Wong, and B. Hewakandamby. Examining the effect of flow rate ratio on droplet generation and regime transition in a microfluidic T-junction at constant capillary numbers. *Inventions*, 3(54):1–17, 2018. doi: 10.3390/inventions3030054.

[30] I. Chakraborty, J. Ricouvier, P. Yazhgur, P. Tabeling, and A. M. Leshansky. Droplet generation at Hele-Shaw microfluidic T-junction. *Physics of Fluids*, 31(2):1–14, 2019. ISSN 10897666. doi: 10.1063/1.5086808.

[31] M. De Menech, P. Garstecki, F. Jousse, and H. A. Stone. Transition from squeezing to dripping in a microfluidic T-shaped junction. *Journal of Fluid Mechanics*, 595:141–161, 2008. doi: 10.1017/S002211200700910X.

[32] H. Liu and Y. Zhang. Droplet formation in a T-shaped microfluidic junction. *Journal of Applied Physics*, 106(3):1–20, 2009. doi: https://doi.org/10.1063/1.3187831.

[33] A. Gupta and R. Kumar. Flow regime transition at high capillary numbers in a microfluidic T-junction: Viscosity contrast and geometry effect. *Physics of Fluids*, 22(12):1–11, 2010. ISSN 10706631. doi: 10.1063/1.3523483.

[34] A. Gupta and R. Kumar. Effect of geometry on droplet formation in the squeezing regime in a microfluidic T-junction. *Microfluidics and Nanofluidics*, 8(6):799–812, 2010. ISSN 16134982. doi: 10.1007/s10404-009-0513-7.

[35] J. Sivasamy, T. N. Wong, N. T. Nguyen, and L. T. H. Kao. An investigation on the mechanism of droplet formation in a microfluidic T-junction. *Microfluidics and Nanofluidics*, 11(1):1–10, 2011. ISSN 16134982. doi: 10.1007/s10404-011-0767-8.

[36] X. B. Li, F. C. Li, J. C. Yang, H. Kinoshita, M. Oishi, and M. Oshima. Study on the mechanism of droplet formation in T-junction microchannel. *Chemical Engineering Science*, 69(1):340–351, 2012. ISSN 00092509. doi: 10.1016/j.ces.2011.10.048.

[37] J. H. Xu, G. S. Luo, S. W. Li, and G. G. Chen. Shear force induced monodisperse droplet formation in a microfluidic device by controlling wetting properties. *Lab on a Chip*, 6(1):131–136, 2006. ISSN 14730189. doi: 10.1039/b509939k.

[38] D. Sampaio. Caracterização experimental da camada de plasma em escoamentos de sangue animal no interior de microcanais com promotores de mistura em zigzag. MSC thesis. Mechanical Engineering Department, Instituto Superior Tecnico, University of Lisbon,. 2016.

[39] M. Chinaud, M. J. Simmons, E. Nowak, P. Angeli, N. M. Kovalchuk, and E. Roumpea. Effect of surfactant on emulsification in microchannels. *Chemical Engineering Science*, 176:139–152, 2017. ISSN 00092509. doi: 10.1016/j.ces.2017.10.026.

[40] K. Wang, Y. C. Lu, J. H. Xu, and G. S. Luo. Determination of dynamic interfacial tension and its effect on droplet formation in the T-shaped microdispersion process. *Langmuir*, 25(4):2153–2158, 2009. ISSN 07437463. doi: 10.1021/la803049s.

[41] H. Liu and Y. Zhang. Droplet formation in microfluidic cross-junctions. *Physics of Fluids*, 23(8): 1–12, 2011. ISSN 10706631. doi: 10.1063/1.3615643.

[42] S. M. S. Murshed, S. H. Tan, and N. T. Nguyen. Temperature dependence of interfacial properties and viscosity of nanofluids for droplet-based microfluidics. *Journal of Physics D: Applied Physics*, 41(8):1–5, 2008. ISSN 00223727. doi: 10.1088/0022-3727/41/8/085502.

[43] S. M. S. Murshed, S. H. Tan, N. T. Nguyen, T. N. Wong, and L. Yobas. Microdroplet formation of water and nanofluids in heat-induced microfluidic T-junction. *Microfluidics and Nanofluidics*, 6(2): 253–259, 2009. ISSN 16134982. doi: 10.1007/s10404-008-0323-3.

[44] S. H. Tan, S. M. Sohel Murshed, N. T. Nguyen, T. N. Wong, and L. Yobas. Thermally controlled droplet formation in flow focusing geometry: Formation regimes and effect of nanoparticle suspension. *Journal of Physics D: Applied Physics*, 41(16):1–7, 2008. ISSN 00223727. doi: 10.1088/0022-3727/41/16/165501.

[45] S. Murshed and N.-T. Nguyen. *Nanofluids: Synthesis, Properties and Applications. Nanofluids in droplet-based microfluidics*. Nova Science Publishers, Inc., 2014. ISBN 9781633216846 — 9781633216778.

[46] I. Mahbubul. *Preparation, Characterization, Properties and Application of Nanofluid. Preparation of Nanofluid*. Elsevier - Micro & Nano Technologies Series, 2019. ISBN 9780128132456. doi: 10.1016/b978-0-12-813245-6.00002-2.

[47] S. Yeom and S. Y. Lee. Dependence of micro-drop generation performance on dispenser geometry. *Experimental Thermal and Fluid Science*, 35(8):1565–1574, 2011. ISSN 08941777. doi: 10.1016/j.expthermflusci.2011.07.008.

[48] J. S. Taurozzi, V. A. Hackley, and M. R. Wiesner. Preparation of nanoparticle dispersions from powdered material using ultrasonic disruption (NIST Special Publication 1200-2). 2012. doi: https://doi.org/10.6028/NIST.SP.1200-2.

[49] Y. Xia and G. M. Whitesides. Soft Lithography. *Annual Review of Materials Science*, 28(1):153–184, 1998. ISSN 0084-6600. doi: 10.1146/annurev.matsci.28.1.153.

[50] S. R. Quake and A. Scherer. From micro to nanofabrication with soft materials. *Science*, 290: 1536–1540, 2000. doi: 10.1126/science.290.5496.1536.

[51] J. A. Rogers and R. G. Nuzzo. Recent progress in soft lithography. *Materials Today*, 8(2):50–56, 2005. ISSN 13697021. doi: 10.1016/s1369-7021(05)00702-9.

[52] J. C. Mcdonald, D. C. Duffy, J. R. Anderson, D. T. Chiu, H. Wu, O. J. A. Schueller, and G. M. Whitesides. Fabrication of microfluidic systems in poly(dimethylsiloxane). *Electrophoresis*, 21:27–40, 2000.

[53] MicroChem. "SU-8 50 and 100: Negative Tone Photoresist". 2002. doi: http://www.microchem.com/pdf/SU8_50-100.pdf.

[54] S. A. Peixoto. Estudo experimental da mistura de fluidos newtonianos em micromisturadores do tipo T com obstáculos de geometria variável para diferentes razões de caudais de entrada. MSC thesis. Mechanical Engineering Department, Instituto Superior Tecnico, University of Lisbon,. 2019.

[55] C. T. Nguyen, F. Desgranges, N. Galanis, G. Roy, T. Maré, S. Boucher, and H. Angue Mintsa. Viscosity data for Al_2O_3-water nanofluid-hysteresis: is heat transfer enhancement using nanofluids reliable? *International Journal of Thermal Sciences*, 47(2):103–111, 2008. ISSN 12900729. doi: 10.1016/j.ijthermalsci.2007.01.033.

[56] J. Kim, M. K. Chaudhury, M. J. Owen, and T. Orbeck. The mechanisms of hydrophobic recovery of polydimethylsiloxane elastomers exposed to partial electrical discharges. *Journal of Colloid and Interface Science*, 207:200–207, 2001. doi: 10.1006/jcis.2001.7909.

[57] Y. Berdichevsky, J. Khandurina, A. Guttman, and Y. H. Lo. UV/ozone modification of poly(dimethylsiloxane) microfluidic channels. *Sensors and Actuators, B: Chemical*, 97(2-3):402–408, 2004. ISSN 09254005. doi: 10.1016/j.snb.2003.09.022.

[58] S. Bhattacharya, A. Datta, J. M. Berg, and S. Gangopadhyay. Studies on surface wettability of poly(dimethyl)siloxane (PDMS) and glass under oxygen-plasma treatment and correlation with bond strength. *Journal of Microelectromechanical Systems*, 14(3):590–597, 2005.

[59] M. Sun, S. S. Bithi, and S. A. Vanapalli. Microfluidic static droplet arrays with tuneable gradients in material composition. *Lab on a Chip*, 11(23):3949–3952, 2011. ISSN 14730189. doi: 10.1039/c1lc20709a.

[60] Y. N. Cheung, N. T. Nguyen, and T. N. Wong. Droplet manipulation in a microfluidic chamber with acoustic radiation pressure and acoustic streaming. *Soft Matter*, 10(40):8122–8132, 2014. ISSN 17446848. doi: 10.1039/c4sm01453g.

[61] H. D. Xi, W. Guo, M. Leniart, Z. Z. Chong, and S. H. Tan. AC electric field induced droplet deformation in a microfluidic T-junction. *Lab on a Chip*, 16(16):2982–2986, 2016. ISSN 14730189. doi: 10.1039/c6lc00448b.

[62] D. S. Zhu, S. Y. Wu, and N. Wang. Surface tension and viscosity of aluminum oxide nanofluids. *AIP Conference Proceedings*, 1207:460–464, 2010. ISSN 0094243X. doi: 10.1063/1.3366409.

[63] M. H. Bhuiyan, R. Saidur, M. A. Amalina, R. M. Mostafizur, and A. K. Islam. Effect of nanoparticles concentration and their sizes on surface tension of nanofluids. *Procedia Engineering*, 105:431–437, 2015. ISSN 18777058. doi: 10.1016/j.proeng.2015.05.030.

[64] T. Gervais, J. El-Ali, A. Günther, and K. F. Jensen. Flow-induced deformation of shallow microfluidic channels. *Lab on a Chip*, 6(4):500–507, 2006. ISSN 14730189. doi: 10.1039/b513524a.

[65] Z. Z. Chong, S. B. Tor, A. M. Gañán-Calvo, Z. J. Chong, N. H. Loh, N. T. Nguyen, and S. H. Tan. Automated droplet measurement (ADM): an enhanced video processing software for rapid droplet measurements. *Microfluidics and Nanofluidics*, 20(4):1–14, 2016. ISSN 16134990. doi: 10.1007/s10404-016-1722-5.

[66] A. S. Basu. Droplet morphometry and velocimetry (DMV): A video processing software for time-resolved, label-free tracking of droplet parameters. *Lab on a Chip*, 13(10):1892–1901, 2013. ISSN 14730189. doi: 10.1039/c3lc50074h.

Appendix A

Technical Datasheets

It is possible to add PDF files to the document, such as technical sheets of some equipment used in the work.

A.1 Viscosimeter

1. Turn on the computer and the viscosimeter, in external mode.
2. Remove and clean the sample cup and cone spindle of the viscosimeter.
3. Open the programme *Rheocalc32*.
4. Perform auto-zero.

   Without the cone spindle and the sample cup, click on the yellow radius located in the dashboard.

   Torque must be at $0.0 \pm 0.1\%$.
5. Insert the cone in the viscosimeter, not damaging the spindle where it connects.

   Push the spindle up with the finger, where the cone is inserted.

   Place the wrench on top of the spindle so it doesnt rotate.

   Release the finger and insert the cone, spinning it clockwise.
6. Turn on the switch above the base. A red light will appear.
7. Insert the sample cup.
8. With the red light, hold the system together with the tension bar and rotate the aligner, between the cup and the switch, counterclockwise. Check the distance between the cone and the cup (a yellow light will show when the hit point is reached).
9. When the yellow light appears, rotate 1 or 2 divisions in the clockwise direction so the cone stops touching the cup and it reaches an optimal distance of measurement.

Note: If the yellow light appears at step 7, the sample cup is touching the spindle. Rotate counterclockwise until it shows red. Perform step 8 and 9.

10. Turn off the toggle switch of step 7.
11. Verify if the torque is at 0.0 $\%$ or 0.1 $\%$. If not, repeat steps from 4 to 10.
12. Remove the sample cup and pour 0.5 mL of working fluid in the center.
13. Place again the sample cup in the viscosimeter.
14. Run the desired routine on the programme.
15. Export results.
16. Remove the cone and sample cup.
17. Clean cone spindle and sample cup with DI water and organize the work place.